Self-lubricious tool coatings for ecological metal cutting

Von der Fakultät für Georessourcen und Materialtechnik
der Rheinisch-Westfälischen Technischen Hochschule Aachen

zur Erlangung des akademischen Grades eines

Doktors der Ingenieurwissenschaften

genehmigte Dissertation

vorgelegt von **M.Sc.**

Thomas Reeswinkel

aus Lüdenscheid

Berichter: Univ.-Prof. Jochen M. Schneider, Ph.D.
Univ.-Prof. Dipl.-Ing. Dr.mont. Christian Mitterer

Tag der mündlichen Prüfung: 19. Januar 2012

Diese Dissertation ist auf den Internetseiten der Hochschulbibliothek online verfügbar

Materials Chemistry Dissertation

No.: 16 (2012)

Thomas Reeswinkel

Self-lubricious tool coatings for ecological metal cutting

Shaker Verlag
Aachen 2012

Bibliographic information published by the Deutsche Nationalbibliothek
The Deutsche Nationalbibliothek lists this publication in the Deutsche Nationalbibliografie; detailed bibliographic data are available in the Internet at http://dnb.d-nb.de.

Zugl.: D 82 (Diss. RWTH Aachen University, 2012)

Copyright Shaker Verlag 2012
All rights reserved. No part of this publication may be reproduced, stored in a retrieval system, or transmitted, in any form or by any means, electronic, mechanical, photocopying, recording or otherwise, without the prior permission of the publishers.

Printed in Germany.

ISBN 978-3-8440-0905-7
ISSN 1861-0595

Shaker Verlag GmbH • P.O. BOX 101818 • D-52018 Aachen
Phone: 0049/2407/9596-0 • Telefax: 0049/2407/9596-9
Internet: www.shaker.de • e-mail: info@shaker.de

Abstract

Transition metal oxide Magnéli phases are traditionally described as crystallographic shear structures. Some of these phases feature a layered crystal structure based on deformed metal–oxygen octahedra. Here, the correlation between structure, decohesion energies and elastic properties of several transition metal oxides is described using *ab initio* calculations. First, seven different vanadium oxides VO_x ($1 \leq x \leq 2.5$) have been investigated. The C_{44} values for V_6O_{13}, V_4O_9, V_3O_7 and V_2O_5 are significantly lower than those for V_2O_3 and VO_2. This is consistent with calculated decohesion energies for cleavage in VO_2 and V_2O_5. When cleaving V_2O_5, decohesion energies are considerably lower than those of VO_2. This behaviour may be understood based on V valency induced changes in the crystal and electronic structure as well as in the chemical bonding. As the V valency is increased, the bond strength decreases. The phases with a V valency $>$4 exhibit low C_{44} values, large anisotropy and possess weak ionic bonding between the layers. The formation of easily plastically deformable structures is enabled by the screened Coulomb potential. The largest distance and therefore weakest bond strength is observed for V_2O_5 in the (002) plane. Studies have then been extended to WO_3, ReO_3, MoO_2, VO_2, V_2O_5 and TiO_2, showing that the decohesion energies and elastic constants C_{44} are inversely proportional to the original distance between the cleaved layers and correspond to the screened Coulomb potential. This can be understood based on the electronic structure. The bond strength decreases rapidly as the distance is increased, resulting in weak coupling between the layers which in turn causes the formation of easily plastically deformable structures, for instance WO_3 or V_2O_5. The fact that structures such as WO_3 can also be described by the above-presented correlations provides the basis for quantum mechanical guided design of Magnéli phase structured solid lubricants, based on tailoring the layer distance by varying the chemical composition.

A combinatorial method was employed to grow TiAlN–WN_x films by DC sputtering as well as by High Power Pulsed Magnetron Sputtering (HPPMS) where the W concentration was varied between 10 to 52 at.% and 7 to 54 at.%, respectively. Experiments were paired with *ab initio* calculations to investigate the correlation between composition, structure and mechanical properties. As the W concentration was increased, the lattice parameter of cubic TiAlN–WN_x films first increased and then decreased for W concentrations above $\approx$29 at.%

(DCMS) and $\approx$27 at.% (HPPMS) as the N concentration decreased. Calculations helped to attribute the increase to the substitution of Ti and Al by W and the decrease to the presence of N vacancies. Young's modulus and hardness were around 385 to 400 GPa and 29 to 31 GPa for DCMS and 430 to 480 GPa and 34 to 38 GPa for HPPMS, respectively, showing no significant trend as the W concentration was increased, whereas calculations showed a continuous decrease in Young's modulus from 440 to 325 GPa as the W concentration was increased from 0 to 37.5 at.%. The presence of N vacancies was shown to increase the calculated Young's modulus. Hence, the relatively constant values measured may be understood based on N vacancy formation as the W concentration was increased. HPPMS-deposited films exceeded DCMS films in Young's modulus and hardness, which may be a consequence of the larger degree of ionisation in the HPPMS plasma. It is reasonable to assume that especially the ionised film forming species may contribute towards film densification and N vacancy formation.

Zusammenfassung

Übergangsmetalloxid-Magnéliphasen lassen sich als kristallografische Scherstrukturen beschreiben. Einige dieser Phasen besitzen eine geschichtete Kristallstruktur aus deformierten Metall–Sauerstoff-Oktaedern. In dieser Arbeit wird mit Hilfe von *ab initio*-Berechnungen der Zusammenhang zwischen Struktur, Spaltungsenergie und elastischen Eigenschaften einiger Übergangsmetalloxide beschrieben. Zunächst sind sieben verschiedene Vanadiumoxide VO_x ($1 \leq x \leq 2.5$) untersucht worden. Die C_{44}-Werte für V_6O_{13}, V_4O_9, V_3O_7 und V_2O_5 sind deutlich niedriger als die für V_2O_3 und VO_2. Dieser Unterschied steht im Einklang mit den berechneten Spaltungsenergien (Dekohäsionsenergien) für verschiedene Kristallebenen, die für V_2O_5 ebenfalls beträchtlich niedriger sind als für VO_2. Dieses Verhalten kann durch die vanadiumvalenzinduzierten Änderungen in der Kristall- und elektronischen Struktur sowie in den chemischen Bindungen verstanden werden. Mit steigender Vanadiumvalenz nimmt die Bindungslänge zu. Phasen mit Vanadiumvalenz $>$4 zeigen niedrige C_{44}-Werte, hohe Anisotropie und besitzen nur schwache ionische Bindungen zwischen den Ebenen. Durch das abgeschirmte Coulomb-Potential wird die Bildung von leicht plastisch verformbaren Strukturen ermöglicht. Der größte Abstand und damit die schwächste Bindung wird bei V_2O_5 in der (002)-Ebene beobachtet. Bei Ausdehnung der Untersuchungen auf WO_3, ReO_3, MoO_2, VO_2, V_2O_5 und TiO_2 hat sich gezeigt, dass die Spaltungsenergien und elastischen Konstanten C_{44} umgekehrt proportional zum ursprünglichen Abstand zwischen den gespaltenen Ebenen sind. Dieses Verhältnis kann durch das abgeschirmte Coulomb-Potential beschrieben werden und lässt sich durch die elektronische Struktur erklären. Die Bindungsstärke nimmt mit zunehmendem Abstand rapide ab, woraus sich eine nur schwache Kopplung zwischen den Ebenen ergibt, welche dann zur Bildung leicht plastisch verformbarer Strukturen wie zum Beispiel WO_3 oder V_2O_5 führt. Der Umstand, dass Strukturen wie WO_3 auch durch die oben genannten Zusammenhänge beschrieben werden können, bildet die Grundlage für ein quantenmechanisch geführtes Design von auf Magnéliphasen basierenden Festschmierstoffen, bei denen der Ebenenabstand durch Verändern der chemischen Zusammensetzung maßgeschneidert werden kann.

Unter Verwendung eines kombinatorischen Ansatzes sind TiAlN–WN_x-Dünnschichten durch DC Magnetron Sputtering (DCMS) sowie High Power Pulsed Magnetron Sputtering (HPPMS) abgeschieden worden. Die so hergestellten Schichten weisen Wolfram-Konzentrationen von 10 bis 52 at.% beziehungswei-

se 7 bis 54 at.% auf. Diese Experimente wurden durch *ab initio*-Berechnungen unterstützt, um den Zusammenhang zwischen Zusammensetzung, Struktur und mechanischen Eigenschaften zu untersuchen. Bei Erhöhung der W-Konzentration nimmt der Gitterparameter der kubischen TiAlN–WN_x-Schicht zunächst zu, nimmt dann aber bei W-Konzentrationen oberhalb von $\approx$29 at.% (DCMS) beziehungsweise $\approx$27 at.% (HPPMS) wieder ab, wie auch die N-Konzentration abnimmt. Mit Hilfe der Berechnungen konnte die Zunahme des Gitterparameters der Substitution von Ti und Al durch W und die Abnahme dem Auftreten von Stickstoff-Leerstellen zugeschrieben werden. Elastizitätsmodul und Härte der Dünnschichten betrugen 385 bis 400 GPa und 29 bis 31 GPa für DCMS beziehungsweise 430 bis 480 GPa und 34 bis 38 GPa für HPPMS. Mit Erhöhung der W-Konzentration war hier kein eindeutiger Trend erkennbar, wohingegen die Berechnungen eine kontinuierliche Abnahme des Elastizitätsmoduls von 440 auf 325 GPa zeigten, wenn die W-Konzentration von 0 auf 37,5 at.% erhöht wurde. Der Einbau von Stickstoff-Leerstellen führte zu einer Erhöhung des berechneten Elastizitätsmoduls. Die relativ gleichbleibenden experimentellen Werte können daher durch das Auftreten von N-Leerstellen erklärt werden, die sich bei Erhöhung der W-Konzentration bilden. Die mittels HPPMS abgeschiedenen Schichten übertreffen die DCMS-Schichten an Elastizitätsmodul und Härte, was auf den größeren Ionisationsgrad des HPPMS-Plasmas zurückzuführen sein könnte. Es ist anzunehmen, dass insbesondere die ionisierten schichtbildenden Teilchen zur Verdichtung der Schicht und zur Bildung von N-Leerstellen beitragen.

Preface

The work presented in this thesis is the summary of research performed at Materials Chemistry of RWTH Aachen University. The work was part of the project “ÖkoZer” (“Lubricating nano composites for ecological cutting operations”, FKZ: 03X3507C), funded by the Federal Ministry of Education and Research of the Federal Republic of Germany and their framework programme “materials innovations for industry and society” (“Werkstoffinnovationen für Industrie und Gesellschaft – WING”), represented by Projektträger Jülich.

Publications

Papers contributing to this thesis

Paper I

***Ab initio* calculations of the structure and mechanical properties of vanadium oxides**
Thomas Reeswinkel, Denis Music and Jochen M. Schneider
Journal of Physics: Condensed Matter 21, 145404 (8pp) (2009)

Paper II

Coulomb-potential-dependent decohesion of Magnéli phases
Thomas Reeswinkel, Denis Music and Jochen M. Schneider
Journal of Physics: Condensed Matter 22, 292203 (4pp) (2010)

Paper III

Structure and mechanical properties of TiAlN–WN$_x$ thin films
Thomas Reeswinkel, Davide G. Sangiovanni, Valeriu Chirita, Lars Hultman and Jochen M. Schneider
Surface and Coatings Technology 205(20), 4821–4827 (2011)

Papers related to this thesis

Paper IV

Structure, elastic properties and phase stability of $Cr_{1-x}Al_xN$

Paul H. Mayrhofer, Denis Music, Thomas Reeswinkel, Hans-Gerd Fuß and Jochen M. Schneider

Acta Materialia 56, 2469–2475 (2008)

Other publications

Paper V

Synthesis and structural characterization of BaV_4O_9

Thomas Reeswinkel, Sebastian Prinz, Karine M. Sparta and Georg Roth

Acta Crystallographica Section B 63, 270–276 (2007)

Paper VI

$Ba_3Li_2V_2O_7Cl_4$, a new vanadate with a channel structure

Thomas Reeswinkel, Karine M. Sparta and Georg Roth

Acta Crystallographica Section C 64, i38–i40 (2008)

Paper VII

Immobilized DNA aptamers used as potent attractors for porcine endothelial precursor cells

Jan Hoffmann, Angela Paul, Marc Harwardt, Jürgen Groll, Thomas Reeswinkel, Doris Klee, Martin Möller, Heike Fischer, Tobias Walker, Tim Greiner, Gerhard Ziemer and Hans P. Wendel

Journal of Biomedical Materials Research Part A 84A, 614–621 (2008)

Acknowledgements

This work would not have been possible without the support of some other people that I would like to thank:

First of all, my supervisor **Univ.-Prof. Jochen M. Schneider, Ph.D.**, for giving me the opportunity to carry out research in his group and work on this interesting topic. I am grateful for your support, guidance and feedback.
Univ.-Prof. Dipl.-Ing. Dr.mont. Christian Mitterer, for your willingness to act as the reviewer, the interesting exchange with you and your research group in Leoben and the great workshops.
Denis, for sharing your knowledge on DFT with me, corrections on my manuscripts, endless support and for switching on the light at the end of the tunnel when needed.
Davide G. Sangiovanni, **Valeriu Chirita** and **Lars Hultman**, from the fellow Linköping group, for the fruitful collaboration on the nitride topic.
Carolin Hostert, **Jie Zhang** and **Denis Music**, for your support on the SEM images.
Manfred Kaiser, **Bernd Conrad**, **Dieter Horbach**, **Stefan Dondorf** and the whole **electronic lab and machine shop team**, for helping to make my ideas of experiments become reality. **Manfred**, I enjoyed the moments you shared your worldly wisdoms.
My bachelor student **Stefanie**, for the assistance on lots of experiments.
The *wise guys*, for sharing their knowledge and experience with me. **Stano**, I always enjoyed travelling with you. **Jens**, I don't think I ever caught you bad-tempered.
My old office mates **Adil**, **Jenny**, **Helmut** and **Ahmed**, as well as **Darwin**, for all the fun we had, deep discussions and your friendship.
Tetsuya, my new desk mate, for all the discussions burning the midnight oil and your great attitude.
Carolin, for sharing the student advisory service in good times and bad, and for cat content.
Michaela and **all the other people in the institute**, for the cordial atmosphere.

. . . and, most importantly, **my family**, for your endless and unconditional support, encouragement and love. You are always by my side, wherever I may be.

Contents

1 Introduction **1**
1.1 Motivation . . . 1
1.2 Literature review . . . 3
1.2.1 Titanium nitride-based coatings . . . 3
1.2.2 Magnéli phase oxides . . . 6
1.3 Goal and strategy . . . 10

2 Theoretical and experimental methods **15**
2.1 Theoretical methods . . . 15
2.1.1 Density functional theory . . . 15
2.1.2 *Ab initio* calculation methods as applied here . . . 17
2.2 Experimental methods . . . 22
2.2.1 Thin film deposition . . . 22
2.2.2 Experimental set-up for thin film depositions . . . 27
2.2.3 Scanning electron microscopy . . . 30
2.2.4 Energy-dispersive X-ray spectroscopy . . . 31
2.2.5 X-ray diffraction . . . 32
2.2.6 Nanoindentation . . . 34

3 Results and discussion **37**
3.1 *Ab initio* calculation of vanadium oxides . . . 37
3.1.1 Crystal structure . . . 37
3.1.2 Energy of formation . . . 40
3.1.3 Elastic properties . . . 40
3.1.4 Decohesion energies . . . 44
3.1.5 Electron density distribution . . . 46
3.1.6 Conclusions . . . 49
3.2 *Ab initio* calculation of Magnéli phase oxides . . . 50
3.2.1 Crystal structure . . . 50
3.2.2 Coulomb-potential-dependent decohesion of Magnéli phases 53
3.2.3 Conclusions . . . 57

3.3 TiAlN–WN_x thin film deposition 58
3.3.1 Thin film morphology and deposition rates 58
3.3.2 Thin film composition 60
3.3.3 Thin film structure and lattice parameter 62
3.3.4 Young's modulus and hardness of the thin films 67
3.3.5 Conclusions 70

4 Conclusions **73**
4.1 Magnéli phase oxides conclusions 73
4.2 TiAlN–WN_x conclusions 74

5 Bibliography **77**

A *Ab initio* calculation methods applied for nitrides **89**

List of Figures

1.1 Crystal structure of TiN. 4
1.2 TiN_x lattice parameter vs. N/Ti ratio. 4
1.3 Crystal structure of ReO_3. 9
1.4 Crystal structure of V_2O_5. 9
1.5 V–O phase diagram. 11
1.6 W–O phase diagram. 11
1.7 Section of the W–O phase diagram. 12
2.1 Correlation of C_{44} and G. 20
2.2 Simplified sputtering system and mechanisms. 23
2.3 Schematic synthesis strategy. 28
2.4 Cathode voltage and current during deposition. 29
2.5 SEM scheme (with EDX). 31
2.6 XRD scheme: Bragg diffraction. 33
2.7 Load–displacement curve. 35
3.1 B and C_{44} as a function of vanadium valency. 43
3.2 B/C_{44} ratio as a function of vanadium valency. 43
3.3 G as a function of the distance between the cleaved blocks. 45
3.4 G as a function of the layer distance. 46
3.5 Electron density distribution of V_2O_3 and VO_2. 47
3.6 Electron density distribution of V_6O_{13}, V_3O_7 and V_2O_5. 48
3.7 G and C_{44} as a function of the layer distance. 54
3.8 Electron density distribution of ReO_3, WO_3 and V_2O_5. 56
3.9 Cross-section images of the TiAlN–WN_x films. 59
3.10 Composition of the deposited films. 61
3.11 Diffraction patterns of the deposited films. 63
3.12 Lattice parameter of TiAlN–WN_x films. 65
3.13 Young's modulus and hardness of the deposited films. 68

List of Tables

2.1 Deposition conditions for DCMS and HPPMS. 29
3.1 VO cell description. 37
3.2 V_2O_3 cell description with hexagonal axes. 38
3.3 VO_2 cell description. 38
3.4 V_6O_{13} cell description. 38
3.5 V_4O_9 cell description. 39
3.6 V_3O_7 cell description. 39
3.7 V_2O_5 cell description. 39
3.8 Calculated properties of the vanadium oxides. 42
3.9 Decohesion energies for VO_2 and V_2O_5. 44
3.10 WO_3 P 4/n c c Z cell description. 50
3.11 WO_3 P 4/n m m Z cell description. 51
3.12 WO_3 P $\bar{4}\,2_1$ m cell description. 51
3.13 WO_3 P c n b cell description. 51
3.14 WO_3 P m n b cell description. 51
3.15 WO_3 P 4/n c c Z cell description. 52
3.16 TiO_2 (rutile) cell description. 52
3.17 MoO_2 cell description. 52
3.18 Calculated data for VO_2, V_2O_5, MoO_2 and five WO_3 phases. . . . 55
3.19 Calculated lattice parameter, bulk, Young's and shear modulus for nitrides. 69

1 Introduction

The properties and performance of a material depend on several factors, most influencing its composition and microstructure. In the field of materials science, the correlation between synthesis, structure, properties and performance of materials is systematically investigated to improve and/or tailor material properties. One possibility to improve the performance of a material is to combine two or more materials within one component. Thus, the characteristics of those materials can be combined to result in a better performance than either one of the individual materials. Often, such material combinations are realised as a relatively thin layer on a bulk material. Examples are zinc galvanising of steel to increase the oxidation resistance but keep the steel's strength and toughness, non-stick Teflon coatings on frying pans or decorative chromium layers on plastic or brass fittings. One method to produce multi-material components is thin film technology based on vapour phase condensation, where layers of different materials can be deposited on the base material, the substrate. Here, atoms, ions, molecules or clusters are deposited at pressures much lower than the atmospheric pressure. Depending on the application, typical thicknesses range from atomic layers to several µm. Physical vapour deposition is a widespread method to grow thin films, e.g. to deposit electrically conductive layers as the contact on a semiconductor device or hard coatings on components or tools for wear and/or oxidation protection to enhance the tool life. One of these tool coating materials is titanium aluminium nitride. While wear and oxidation protection have been investigated, research and development activities geared towards alloying concepts for self-lubrication are often of empirical nature.

The ambition of this work is to contribute towards the scientific background and understanding required to enable a knowledge-based design of self-lubricating tool coatings.

1.1 Motivation

Thin films explored in this thesis are used as wear protection coatings for metal cutting applications to enhance the tool life. For several years, the ma-

terial of choice for industry has been titanium nitride-based, especially titanium aluminium nitride. In the past, the major research and development focus has been placed on higher hardness and higher wear resistance. Since the applied forces in the cutting process influence the work-piece quality and the cost-effectiveness, and especially since more and more ecological aspects are being considered, other tool properties were addressed, too. One major goal is the reduction of lubricating and cooling agents (LCA) to eventually enable a completely dry machining process. The liquid agents typically used have several functions: They lubricate and cool the cutting contact and enable a free chip flow. Adherent chips may cause accumulation of debris which may in turn jam the drill's groove. In addition, tearing off the built-up edge due to adherent chips leads to rapid degradation of the coated tool. Here, lubricating and cooling agents are envisioned to be replaced by solid lubricants incorporated into a hard coating. The strategy is to alloy $(Ti_{1-x}Al_x)N$ with V, W and Mo in such a way that the alloying elements form so-called Magnéli phase oxides, since some of these phases possess low friction coefficients and therefore can act as solid lubricants. Hence, tool life will be elongated and due to the reduction of LCA, the environment will be protected as well as efficiency and effectiveness will be increased.

This work was funded by the Federal Ministry of Education and Research of the Federal Republic of Germany within the framework programme "materials innovations for industry and society" ("Werkstoffinnovationen für "Industrie und Gesellschaft – WING"), which was announced in 2003 [1]. Within the "ÖkoZer" project (FKZ: 03X3507, "Lubricating nano composites for ecological cutting operations"), the correlation between composition, structure, mechanical properties and cutting performance of cutting tools coated with cubic $(Ti_{1-x}Al_x)N$ with addition of V, W, Mo and B was investigated in collaboration with industry. Materials Chemistry of RWTH Aachen University was responsible for density functional theory-based *ab initio* calculations to identify Magnéli phases that could act as solid lubricants and to deposit (Ti,Al,X)N (X = {V, W, Mo}) thin films in lab scale, while CemeCon AG was responsible for corresponding depositions in industrial scale to coat tools and for industry-suitable target development. Wolf Werkzeugtechnologie GmbH finally tested these coated tools under real conditions and improved the tool design. The CemeCon AG (Würselen) is a contract coater as well as a coating machine manufacturer, whilst the Wolf Werkzeugtechnologie GmbH (Bruchmühlbach-Miesau), part of the Wolf group, produces drills and milling cutters.

1.2 Literature review

1.2.1 Titanium nitride-based coatings

The titanium–nitrogen phase diagram consists of several phases [2], among them rutile structured Ti_2N [3], but the dominating phase is TiN. The mineral name is Osbornite. TiN is electrically conductive and appears in golden colour. TiN forms in the cubic B1 structure like rock salt (NaCl), space group F m$\overline{3}$m (225), as displayed in Figure 1.1. The lattice parameter a is about 4.24 Å [2, 4, 5]. Lower a values have been reported due to the presence of vacancies on the nitrogen sub-lattice [2, 6–8], e.g. 4.224 Å for $TiN_{0.69}$ [8] or 4.221 Å for $TiN_{0.61}$ [7]. This interpretation has been supported by *ab initio* calculations [9]. For phases with over-stoichiometric N, a decrease in the lattice parameter was attributed to be due to vacancies on the metal sub-lattice [10–12], e.g. 4.213 Å for $TiN_{1.16}$ [12]. Figure 1.2 from Nagakura *et al.* [7] shows the dependence of the lattice parameter of under- and over-stoichiometric TiN_x on x. However, over-stoichiometric N concentrations may also be accommodated by N incorporation at interstitial positions and hence lattice parameters that exceed the common value for bulk samples are reported [6, 8, 13, 14], too, e.g. 4.252 Å for $TiN_{1.17}$ [8] or 4.28 Å for $TiN_{1.18}$ [14]. While decreased a values due to vacancies in the metal sub-lattice are mainly reported for bulk samples [6, 12], interstitial N incorporation is often observed for titanium nitride-based thin films and thus for non-equilibrium film growth conditions [6, 8, 13, 14], but also nitrogen-deficient thin films can be obtained [15]. For sputtered thin films, cubic TiN could be obtained within Ti:N ratios of 0.6 to 1.63, depending on the deposition conditions, especially the nitrogen (partial) pressure [7, 16].

Cubic titanium nitride coatings are known to exhibit high hardness, good wear resistance and relatively low friction and are thus used as hard coatings for metal cutting [17–19]. TiN is also used as a diffusion barrier coating in microelectronic devices [20, 21]. High-temperature application of TiN is limited because of its oxidation behaviour [22, 23]. Adding aluminium, the oxidation resistance and thus wear performance can be greatly increased [23–28]. Due to the previously reported excellent wear resistance, $Ti_{1-x}Al_xN$, (Ti,Al)N or short TiAlN is the bench mark coating for many metal cutting applications today. By the (partial) substitution of Ti by Al, a protective aluminium oxide layer is formed at the surface which inhibits further oxidation [23–28]. While the Al solubility is limited at equilibrium conditions, TiAlN thin films exist over a broad range

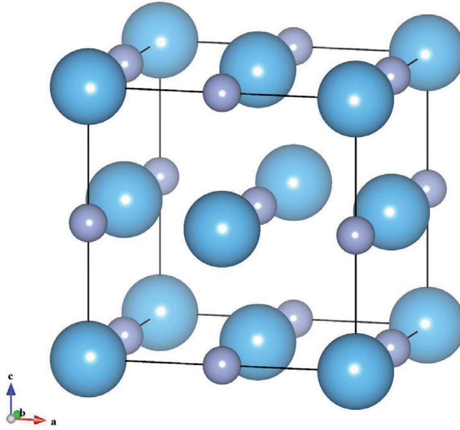

Figure 1.1: Crystal structure of cubic TiN, B1 structure. Ti is shown as blue, N as violet spheres. The unit cell is marked by the black line.

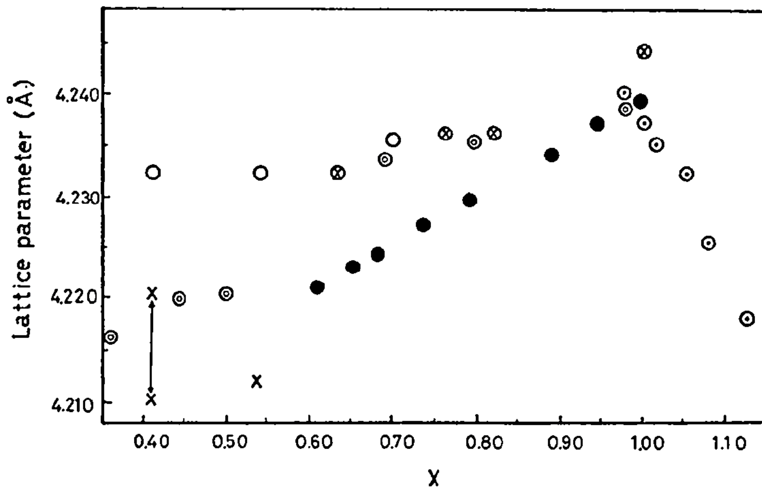

Figure 1.2: Lattice parameter of TiN_x in dependence on the N/Ti ratio x, from Nagakura *et al.* [7]. However, over-stoichiometric interstitial N can also lead to higher a values.

of aluminium concentration. The solubility limit of Al in metastable TiAlN thin films has been investigated theoretically [29–31] and experimentally [32–34]. It was possible to substitute up to about two thirds of Ti by Al within the cubic B1 phase. At higher Al concentrations, hexagonal AlN has been detected. *Ab initio* calculations have shown that the phase stability of $Ti_{1-x}Al_xN$ is not only dependent on the composition but also on the Al distribution within the metal sub-lattice. A maximum solubility of $x = 0.74$ was obtained when both elements were clustered, reducing the number of Ti–Al bonds [35]. When substituting Al for Ti, the lattice parameter decreases, closely following Vegard's law [24, 36–38]. For example, the lattice parameter decreased from 4.247 to 4.209 Å as the Al concentration was increased from 0 to 41 at.% [37]. Similarly, *ab initio* calculations for $Ti_{1-x}Al_xN$ showed a linear decrease of the lattice parameter from 4.27 to 4.14 Å for the AlN fraction x up to $x = 0.7$ based on the rules of mixture [38]. Since the stiffness of the hexagonal phase is lower [39], too high aluminium contents are being avoided. Hence, the optimum composition is described by a high aluminium concentration just below the solubility limit. The bonding within TiN is described as a mixture of ionic, covalent and metallic character [35]. While this is generally maintained for TiAlN, it can be found that the Al–N bonds are more covalent then the Ti–N bonds [35].

As a disadvantage, TiAlN exhibits a larger friction coefficient compared to TiN [36] and a larger wear rate [40]. To enhance the tribological performance of TiAlN coated tools, the effect of alloying elements on the film properties has been investigated, e.g. Y, Cr [41–43] and V [43–47]. During metal cutting in air the surface of the coated tools can be oxidised. Therefore, alloying elements that form solid lubricants have been added to hard coatings. One strategy is to add elements that form so-called Magnéli phase oxides, which can significantly lower the friction coefficient, among them V, Mo and W. Vanadium containing TiAlN has therefore been investigated in the last years, showing a very low friction coefficient when V_2O_5 is formed on the film surface [46, 48]. The friction coefficient could be reduced from about 1 for pure TiAlN to only about 0.2 once vanadium oxide Magnéli phases had been formed on the surface. In particular V_2O_5 was deemed to be the reason for the reduced friction [46, 48–51]. However, due to its low melting point of about 950 K [52–54], V_2O_5 might not be the best candidate for all cutting applications. While the good lubrication is maintained with a film of molten V_2O_5, the liquid material can more easily be removed from the surface [50], e.g. from a drill's surface at high rotation speed.

A decreased friction coefficient has also been reported on tungsten nitride films after WO_3 had been formed on the surface at elevated temperatures [55]. The melting points for tungsten oxides such as WO_3 are significantly higher [56].

Tungsten nitride (WN_x, W_2N) coatings are used as diffusion barrier layers in metallisation schemes in silicon contact structures [57, 58] and as adhesion layers (e.g. between tungsten and silicon) [59]. They have also attracted interest as high-temperature stable Schottky gates for field-effect transistors [60]. Thus, electrical properties such as resistivity or superconducting behaviour are largely discussed in literature [61–64]. The thermodynamically stable phase is W_2N, which can be considered as a TiN-like structure with only half of the nitrogen sites occupied. W_2N refers to a nitrogen concentration of 33 at.%, but a wider stoichiometry range for WN_x has been reported especially for thin films [57, 65] and nitrogen concentrations of 55 at.% [66], 58 at.% [65] and 63 at.% [67] have been observed. The N concentration in WN_x films was reported to depend to a large extent on the deposition conditions, in particular nitrogen pressure, deposition rate and substrate temperature. It has been suggested that in the W_2N structure additional nitrogen occupies the vacant octahedral sites, enlarging the lattice parameter [68, 69]. The lattice parameter for WN_x with $x \approx 1$ was measured to be about 4.28 Å [65, 69], while the value for a stoichiometric W_2N bulk sample is 4.126 Å [JCPDS card No. 25-1257].

1.2.2 Magnéli phase oxides

Transition metal oxide Magnéli phases are traditionally described as crystallographic shear structures that can be derived from the parent perovskite ReO_3 [70–77]. Homologous series within these phase diagrams, often referred to as Magnéli series, have been constructed for vanadium oxides [78–81], such as the V_nO_{2n-1} series between the borderline phases V_2O_3 ($n = 2$) and VO_2 ($n = \infty$) [82] and the V_nO_{2n+1} series between the borderline phases VO_2 ($n = \infty$) and V_2O_5 ($n = 2$) [83], or for tungsten oxides, such as the W_nO_{3n-2} series [72] and the W_nO_{3n-1} series [70]. In addition, there are more than eleven different structures reported for WO_3 [56]. These oxides are of great interest in multiple applications, mainly because of the wide range of valence that is exhibited by the transition metals such as V, W and Mo, which affects the physical and chemical properties of the oxides. A large range of vanadium oxide- [84] or molybdenum oxide-based [85] materials can be used as catalysts, e.g. V_2O_5 for the partial oxidation of ethanol and ethane [86] or the selec-

tive reduction of NO [87]. Several vanadium oxides exhibit a metal-to-insulator phase transition from a high temperature metallic phase to a low temperature insulating or semiconductive phase [88–93]. Here, the V_nO_{2n-1} series is of particular interest [81, 94–97], but also other phases are taken into account [98, 99]. Electrochromism has been reported for VO_2 [100], V_2O_5 [101, 102], MoO_3 [101, 103, 104] and WO_3 [100, 101, 105–107]; thus, these materials are of interest for devices such as smart windows. Some vanadium bronzes, usually non-stoichiometric compounds incorporating (earth) alkali metals, feature interesting magnetic behaviour [108]. Due to the layered structure that facilitates intercalation, V_2O_5, MoO_3 and WO_3 can be used for lithium ion batteries [109]. Tungsten oxides are also used for fireproof fabrics. Some phases are also used as pigments due to their intense colour [110]. Certain Magnéli type oxide phases have been reported to be promising for metal cutting applications [50, 55, 111]. When annealing nitride coatings containing V, W or Mo, the friction coefficient is significantly reduced, due to the formation of lubricious oxide phases such as V_2O_5 [49–51], WO_3 [55] or MoO_3 [55]. Crystal chemistry has been determined to play a major role for the lubricating properties of metal oxides [111]. Density functional theory calculations have been carried out for vanadium oxides, often within the scope of surface studies [112–116], but a systematic correlation between the Magnéli phase (electronic) structure and elasticity as well as decohesion energy has not been explored in the literature.

The "Magnéli phases" are named after the Swedish scientist Arne Magnéli who investigated among other materials molybdenum and tungsten oxides extensively [70, 71, 117–119]. Such transition metal oxides consist of transition metal–oxygen polyhedra MO_6 with octahedral coordination (i.e. including distorted octahedra). A parent structure with perfect MO_6 octahedra is the cubic ReO_3. The structures within the homologous series as mentioned before consist of MO_6 octahedra that can be derived from a parent structure by crystallographic shear, leading to ordered oxygen deficiencies [70–77, 119]. Hence, phases within such series can differ in the absolute stoichiometry and the numbers of shared corners and edges, while the octahedral coordination for the individual metal–oxygen polyhedra is preserved. Two extreme cases are the already mentioned ReO_3 on the one hand, which consists of octahedra that share only corners but no edges, and VO or TiO (rock salt structure) on the other hand, which consists of octahedra that share all edges. The term "crystallographic shear" (CS) is referring to a (geometric) translation of

crystal layers from a base structure, here mainly ReO_3. This way by periodic CS, the stoichiometry of an oxide can be changed without relinquishing the basic metal–oxygen coordination. Based on MO_6 octahedra, numerous CS structures for vanadium, molybdenum and tungsten oxides, often within homologous series, can be constructed such as the V_nO_{2n-1} series [82] and the V_nO_{2n+1} series [83], or for tungsten oxides, such as the W_nO_{3n-2} series [72] and the W_nO_{3n-1} series [70]. Most of the WO_3 phases only differ in the degree of distortion of the WO_6 octahedra [56, 120–123]. The transition metal oxide phases within the scope of this work consist of transition metal–oxygen polyhedra with octahedral coordination related to the ReO_3 structure, e.g. by structural distortion or crystallographic shear. In the following they are described in more detail.

Parent structure ReO_3

Cubic ReO_3, space group $Pm\bar{3}m$ (221), consists of corner-sharing ReO_6 octahedra [124], as displayed in Figure 1.3. The structure can be related to the perovskite ABO_3 prototype, which is based on calcium titanate $CaTiO_3$, with the A site missing [117, 124]. The perfect octahedral coordination in ReO_3 gives rise to six Re–O bonds with the length of 1.89 Å.

Due to this missing A site, there is some degree of freedom for the central transition metal cation (M) to be displaced and for the MO_6 octahedra to be tilted. Thereby, with different degrees of structural distortion, structure variations can be formed. For example, some WO_3 structures can be described as a distorted ReO_3 structure [117]. In the WO_3 $P4/ncc$ Z phase [120], the WO_6 octahedron is distorted and the W cation is shifted from the centre. Thus, different M–O bond lengths are formed. Higher degrees of distortion can lead to the formation of a layered crystal structure. An extremely high degree of MO_6 octahedron distortion can be seen for V_2O_5 [125], where the VO_6 octahedron would rather be described as a VO_5 square pyramid, since the sixth V–O bond length is very large (2.8 Å). In this structure, layers are clearly visible, see Figure 1.4. It must be noted, though, that this structure has a different stoichiometry and is not directly based on ReO_3. It could be described as a zigzag chain arrangement, with some “octahedra” sharing corners while others share edges, derived by crystallographic shear translations [119].

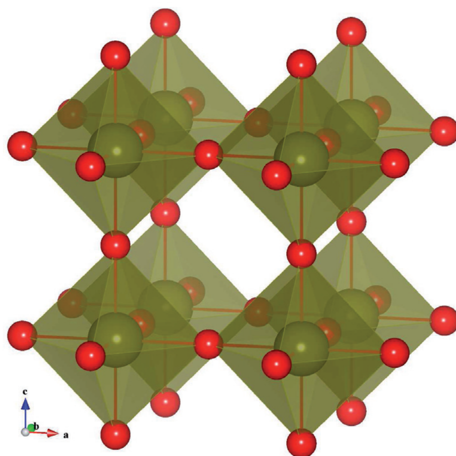

Figure 1.3: Crystal structure of ReO_3 with marked ReO_6 octahedra. Re is shown as green, O as red spheres.

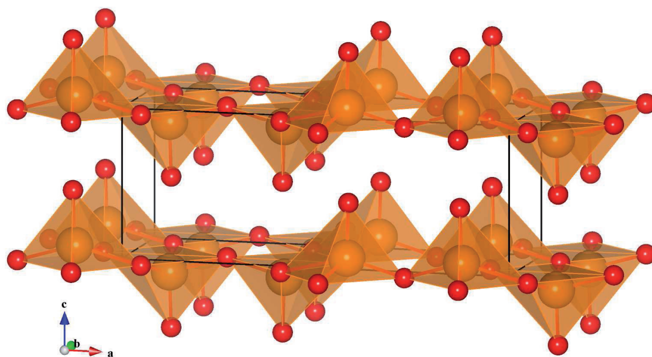

Figure 1.4: Crystal structure of V_2O_5 with the V–O polyhedra shown as VO_5 square pyramids (excluding the longest V–O bond). V is shown as orange, O as red spheres.

Vanadium oxides

The vanadium–oxygen phase diagram showing VO_x with $1 \leq x \leq 2.5$ and thus with vanadium valency from 2 to 5 as drawn from Katzke *et al.* [79] is presented in Figure 1.5. Hence, the phases included range from VO to V_2O_5. The V_nO_{2n-1} series (from V_2O_3 to VO_2) [82] and the V_nO_{2n+1} series (from VO_2 to V_2O_5) [83] can be identified, including V_2O_3 (karelianite, corundum structure) [126], VO_2 (rutile structure) [127], V_6O_{13} [128], V_3O_7 [129] and V_2O_5 (shcherbinaite) [125], as well as VO (rock salt structure) [130]. However, the phase V_4O_9 [131], which is also calculated here, has not been included. As can be seen later, this structure might be considered as being unstable.

Tungsten oxides

The tungsten–oxygen phase diagram, as constructed by Wriedt [56], is presented in Figures 1.6 and 1.7. It is rich of different phases like WO_2, $W_{18}O_{49}$, $W_{24}O_{68}$, WO_3 and homologous series that have been constructed, such as the W_nO_{3n-2} series [72] and the W_nO_{3n-1} series [70]. In addition, there are more than eleven different structures reported for WO_3 [56], most of them just slightly differing in the (degree of) distortion of the WO_6 octahedron [120–123].

1.3 Goal and strategy

With this work, it is my ambition to contribute towards the scientific background and understanding required to enable a knowledge-based design of *self-lubricating* tool coatings. The strategy is to apply *ab initio* calculations to identify transition metal oxides, so-called Magnéli phases, that possess low friction coefficients and therefore can act as solid lubricants, and to alloy TiAlN with these elements by sputter deposition. These Magnéli phase oxides are expected to form on the surface of the as-alloyed TiAlN tool coating during metal cutting processes and provide lubrication without the necessity to use additional, fluid lubricating agents. Thus, more precisely, the objective of this work is to contribute towards understanding the correlation between composition, structure, elastic properties and decohesion energies of transition metal Magnéli phase oxides, namely vanadium, tungsten and molybdenum oxides, and correlate these with the electronic structure thereof. Furthermore, as the second step, the follow up objective is to contribute towards understanding the

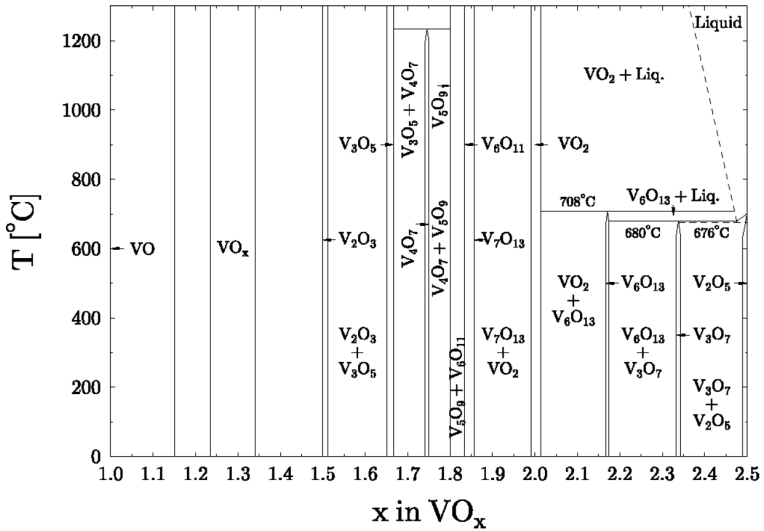

Figure 1.5: Vanadium–oxygen phase diagram showing VO_x in the range $1 \leq x \leq 2.5$, from Katzke *et al.* [79].

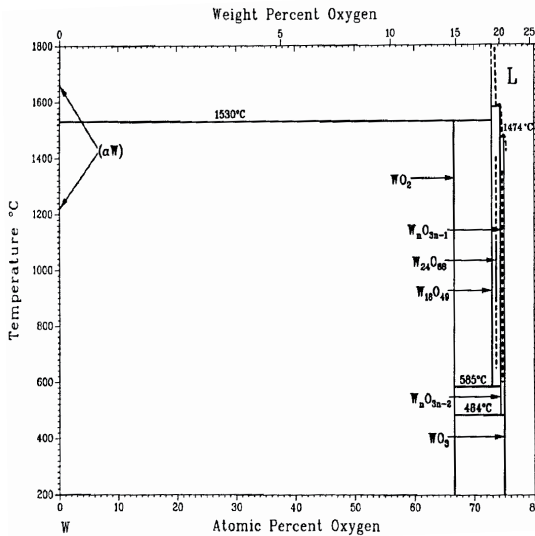

Figure 1.6: Tungsten–oxygen phase diagram from an oxygen concentration of 0 to 75 at.%, from Wriedt [56].

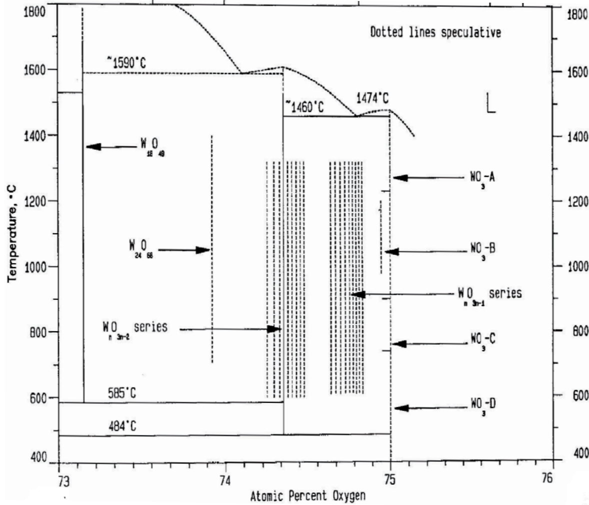

Figure 1.7: A section of the tungsten–oxygen phase diagram in more detail for the oxygen concentration from 73 to 75 at.%, from Wriedt [56].

correlation between composition, structure and mechanical properties of cubic TiAlN alloyed with such Magnéli phase forming elements. Here, tungsten is chosen as a demonstrator, therefore cubic TiAlN–WN$_x$ thin films are investigated.

Quantum mechanical calculations of the structure and properties of materials can be carried out prior to experiments to guide experimental efforts saving time and money. From such calculations, the equilibrium volume and the elastic properties such as the bulk modulus or shear modulus can be obtained. Additionally, information about the electronic structure, such as the density of states, the electron density distribution or the nature of the crystals' bonding are available. Here, density functional theory-based *ab initio* calculations are used to obtain the structure, elastic properties and decohesion energies as well as the electronic structure of Magnéli phase oxides. Hence, correlations between these characteristics can be compiled. Based on these data, Magnéli phase forming elements can be selected for incorporation into a hard coating matrix, such as TiAlN.

For the next step, to alloy TiAlN with additional elements, the method of choice is combinatorial sputtering. With the use of this composition spread method, an efficient screening of different compositions/materials can be performed. Based on a specific arrangement of the deposition system, a broad range of composition within a material system's phase diagram can be covered in one deposition process. This can be fulfilled by two or more cathodes with different elements or by a specially arranged target design, so that the cathode/target geometry results in a chemical gradient on an appropriately placed substrate. Hence, to analyse such films techniques with high lateral resolution are prerequisite. Two different sputtering techniques are employed within this work, namely direct current magnetron sputtering (DCMS) and high power pulsed magnetron sputtering (HPPMS). For conductive targets as employed here, DCMS is the commonly used method. In addition, the HPPMS technique is applied to increase the ionisation of the plasma, in particular of the film-forming species, and thus for a better control of the microstructure evolution.

With respect to future application, it is envisioned that the results obtained here lead to self-lubricating tool coatings that enable dry machining and thus contribute to more ecological processes. With the knowledge gained here, it is intended that industrial partners within the ÖkoZer project are able to produce such coatings in the near future.

2 Theoretical and experimental methods

2.1 Theoretical methods

There are different approaches to model and then calculate and/or simulate the structure, properties and behaviour of materials, which may be summed up as “computational materials science”. One major differentiation that can be made is the scale which is to be modelled, calculated and simulated. They range from macroscopic methods, e.g. finite element method (FEM) for metal forming, over mesoscopic methods, e.g. cellular automata (CA), and microscopic methods, e.g. classical molecular dynamics, to electronic scale, like the quantum mechanical-based methods as applied here. Besides, it can easily be distinguished between the time-independent calculation, e.g. of the electrical conductivity, and the simulation as a function of time, e.g. of the deformation evolution during an indentation process.

“Ab initio” in this context usually refers to *ab initio* quantum mechanical methods, and hence scales at atomistic/electronic level. There are several types, like the Hartree-Fock (HF) techniques or techniques based on the density functional theory (DFT). All have their advantages and disadvantages and hence a preferred area of application. DFT-based calculations are employed in this work.

2.1.1 Density functional theory

In general, to describe the quantum state of a system, what has to be solved is the (time-independent) Schrödinger equation [132]

$$\hat{H}\Psi = E\Psi \tag{2.1}$$

with $\hat{H}$ as the Hamiltonian operator, Ψ as the wave-function and E as the total energy of the system. Walter Kohn was awarded the Nobel Prize in Chemistry in 1998 for his development of the density functional theory. His basic hypothesis was that *a knowledge of the ground-state density of $n(r)$ for any electronic system, (with or without interactions) uniquely determines*

the system [133]. In fact the DFT is based on the two Hohenberg-Kohn (HK) theorems [134]:

- The ground-state energy E_0 of a many-body system is a unique functional of the particle density $n(r)$,

$$E_0 = E[(\vec{r})]. \tag{2.2}$$

- The functional $E[(\vec{r})]$ has its minimum relative to variations of the particle density $\delta n(\vec{r})$ at the equilibrium density $n_0(\vec{r})$,

$$E = E[n_0(\vec{r})] = \min E[(\vec{r})] \tag{2.3}$$

$$\lim_{n(\vec{r}) \to n_0(\vec{r})} \frac{\delta E[n(\vec{r})]}{\delta n(\vec{r})} = 0. \tag{2.4}$$

Including the Hartree equations [135–137] in the HK theory led to the more accurate Kohn-Sham equations [138]. In the end the total-energy functional can be described as

$$E[n] = T[n] + E^H[n] + E^{xc}[n] + \int V(\vec{r})n(\vec{r})\, d^3r \tag{2.5}$$

with $T[n]$ as the kinetic energy term, $E^H[n]$ as the Hartree energy term (electron repulsion), $E^{xc}[n]$ as the exchange and correlation energy term and $V(\vec{r})$ as the external potential term.

The exact form for $E^{xc}[n]$ is unknown. Hence, there are several approximations for the exchange-correlation (XC) energy functional. The local-density approximation (LDA) (solely) takes into account the local electron density at every point in the system, considering a homogeneous density to be existing in the complete system as is found in that particular point [138]. Hence, for strong local variations in the electron density, the result might not be that accurate. To overcome this and other drawbacks, other approximations have been developed. One of those is the generalized-gradient approximation (GGA), which describes the XC term by the electron density and also its local gradient [139]. Accordingly, numerical effort is increased for GGA as compared to LDA. However, it should be kept in mind that, generally, GGA tends to slightly overestimate cell volume compared to LDA, because in many cases LDA overestimates the strength of bonding. But therefore, GGA also tends to

give more accurate values for elastic properties [140]. Further approximations can be made for the atomic potentials, as its behaviour is mainly determined by the valence electrons and direct influence of electrons from the inner shells can be neglected, leading to so-called ultrasoft pseudopotentials [141].

2.1.2 *Ab initio* calculation methods as applied here

In this chapter, information about the DFT-based *ab initio* calculation tools used herein, the *Vienna ab initio simulation package* (VASP), the conditions and settings applied, and how they are used to obtain the crystal structure, energy of formation, elastic properties and electronic structure as well as decohesion energies are explained in detail.

VASP

Calculations in this work were carried out using density functional theory [134] as implemented in the *Vienna ab initio simulation package* (VASP) [142], in which projector augmented wave potentials with the Perdew-Wang (PW91) generalized-gradient approximation are employed [139, 142] with the so-called Blöchl corrections for the total energy [143]. The convergence criterion for the total energy was 0.01 meV within a 500 eV cutoff. Integration in the Brillouin zone was done on special k-points, according to Monkhorst-Pack [144]. All configurations were studied on a mesh of $7 \times 7 \times 7$ irreducible k-points (unless otherwise noted). Equilibrium values for the lattice parameters were obtained by fitting the total energy versus a, b/a or c/a with third order polynomials. All structures were relaxed with respect to atomic positions and Wigner-Seitz primitive cell volume.

Crystal structure calculation

Initial structural data for the *ab initio* calculations were taken from literature for vanadium oxides VO_x $(1 \leq x \leq 2.5)$ with vanadium valency from 2 to 5, including three mixed-valency phases. Namely, these phases are VO (rock salt structure) [130], V_2O_3 (karelianite, corundum structure) [126], VO_2 (rutile structure) [127], V_6O_{13} [128], V_4O_9 [131], V_3O_7 [129] and V_2O_5 (shcherbinaite) [125]. The latter five belong to the V_nO_{2n+1} homologous series between VO_2 $(n = \infty)$ and V_2O_5 $(n = 2)$. As a comparison, α-Al_2O_3 (corundum) [126] and TiO_2 (rutile) [127] as the structural prototypes for V_2O_3 and VO_2, respectively,

were also calculated in the same way. These well-known structures can be used to verify the methodology applied in this work, since relevant experimental data is available. The five phases WO_3 calculated are WO_3 (P 4/n c c Z structure) [120], WO_3 (P 4/n m m Z) [121], WO_3 (P $\bar{4}\,2_1$ m) [122], WO_3 (P c n b) [120] and WO_3 (P m n b) [123]. In addition, a WO_3 parent structure ReO_3 [124] was calculated as well as MoO_2, which is a rutile isostructure like the aforementioned VO_2 and TiO_2.

Energy of formation

To obtain information about the stability of the phases studied, the energy of formation per atom (E_f) with respect to the elements was calculated as the total energy difference between the compound phases probed and the said elements. Equation 2.6 is given as an example for vanadium oxides:

$$E_f(V_xO_y) = \frac{E(V_xO_y) - (x\,E(V) + \frac{1}{2}y\,E(O_2))}{x+y}. \tag{2.6}$$

Thereby, the total energies of bcc vanadium [145] and O_2 were calculated. To obtain the total energy of O_2, a cubic cell was created with one oxygen atom at the cell's origin and another one along the distance of the O=O π-bond length (120.741 pm) [146] in one lattice direction. The lattice parameter was set to 12 Å, anticipating negligible interactions between periodic images.

Elastic properties

The bulk modulus B was obtained by fitting the energy–volume curves to the Birch-Murnaghan equation of states [147], with volume (de)compression of ± 5 and ± 10 %. To calculate elastic properties like Young's modulus E or the shear modulus G, the independent elastic constants C_{ij} are needed. The shear modulus describes the material's response to shearing strains. To calculate its exact value, all independent elastic constants have to be known, which means a high computational effort. The number of independent elastic constants is depending on the crystal symmetry. There are 21 independent elastic constants for a completely asymmetric crystal. With higher symmetry, the number is reduced. A cubic crystal has only three independent elastic constants: C_{11}, C_{12} and C_{44}. The elastic constant for monoclinic strain is C_{44}. C_{44} is proportional to the shear modulus and hence can be used as a measure of

the shear resistance [148, 149]. Thus, computational effort can be significantly reduced. A comparison of the elastic constant C_{44} and the shear modulus G for several cubic and hexagonal structures based on a gathering of experimental data [150] is presented in Figure 2.1, supporting this finding.

The elastic constants are proportional to the second order coefficient of the total energy as a function of the deformation parameter d [151]. The elastic constant C_{44} was determined according to the methods developed by Mehl *et al.* for cubic [152] and tetragonal [153] phases, Ravindran *et al.* [154] for orthorhombic phases and Fast *et al.* [155] for hexagonal phases, with shear stains of ± 1 and $\pm 2\,\%$. An example is given for orthorhombic systems in the following. For orthorhombic crystal structures, there are 9 independent elastic constants. The elastic constant for monoclinic strain C_{44} can be derived by applying a shear deformation according to the strain matrix ϵ given in Equation 2.7 to the respective structure:

$$\epsilon = \begin{pmatrix} \frac{1}{(1-\delta^2)^{1/3}} & 0 & 0 \\ 0 & \frac{1}{(1-\delta^2)^{1/3}} & \frac{\delta}{(1-\delta^2)^{1/3}} \\ 0 & \frac{\delta}{(1-\delta^2)^{1/3}} & \frac{1}{(1-\delta^2)^{1/3}} \end{pmatrix}, \qquad (2.7)$$

with the deformation parameter δ (the degree of deformation). The total energy E associated with this strain is given in Equation 2.8:

$$E(V,\delta) = E(V_0,0) + V_0(2\tau_4\delta + 2C_{44}\delta^2) \qquad (2.8)$$

(with τ_4 being the related element of the stress tensor) [154]. During this deformation, the cell volume V is conserved, so V equals the ground state volume V_0. The energy–volume relation then needs to be solved for term containing the deformation δ and the elastic constant C_{44}. Hence, the second derivative with respect to δ is $2\,C_{44}$.

Due to expectedly large structural anisotropy for some phases, calculations for obtaining B and C_{44} were carried out in two different ways for the vanadium oxides, rutile and corundum:

(i) considering uniform compression (full structural relaxation only at equilibrium and no further relaxations for determination of lattice parameters and elastic constants), and

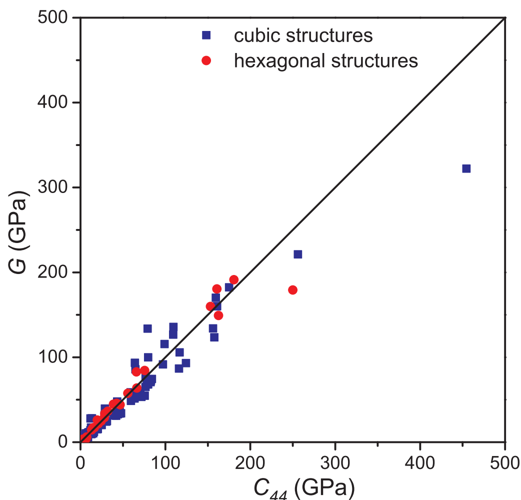

Figure 2.1: Correlation of elastic constant C_{44} and shear modulus G for several materials with cubic and hexagonal crystal structures, showing a linear relationship [150].

(ii) with full structural relaxations at every volume for determination of elastic constants.

The latter procedure yielded more precise results in the case of anisotropic structures, such as hydroxyapatite [156], Nb_2S_2C [157], boron nitrides [158] and graphite [159]. Based on results from the vanadium oxides, succeeding calculations of elastic properties for WO_3 and ReO_3 were (only) carried out with full structural relaxations at every volume.

Electron density distribution

The electron density distribution (EDD) of a calculated structure can be derived from the total charge density data. From EDD images information about bonding within the crystal (or other structures) can be obtained, e.g. charge/electron sharing between atoms. Thus, the EDDs were evaluated to contribute towards understanding of the correlation between the bonding and elastic properties. The EDD data were analysed using the VESTA software [160]. The same settings were applied for each data set to ensure comparability.

Decohesion energy calculation

In order to obtain information about bonding strength to check for easily plastically deformable structures, the decohesion energies for cleavage G were calculated as the energy required for the separation of the structure into two blocks [161, 162]. This energy depends on the cleavage distance between these two separated blocks until it reaches a constant level at a certain distance. No structural relaxation was allowed during the separation [161, 162]. For example, to obtain the (200) cleavage, the cell was cut into two blocks: with one block ranging from fractional coordinate $0 \leq x < 0.5$ (of the original unit cell) and the other ranging from $0.5 \leq x < 1$. Calculations were carried out up to a cleavage distance of 10 Å, at which G remained constant. To avoid interaction between the cleaved planes due to periodic boundary conditions, supercells containing 16 atomic layers normal to the cleavage plane were constructed with a proportionate mesh of irreducible k-points.

For the phases MoO_2, TiO_2, VO_2 and V_2O_5, cleavages were considered in {100} and {200} planes in each (independent) lattice direction. Therefore, in order to cleave MoO_2, TiO_2 and VO_2 in x or symmetrical y direction and in z direction, $3 \times 1 \times 1$ and $1 \times 1 \times 8$ supercells and meshes of $1 \times 5 \times 5$ and $5 \times 5 \times 1$ irreducible k-points were constructed, respectively. To cleave V_2O_5 in x, y and z direction, $3 \times 1 \times 1$, $1 \times 8 \times 1$ and $1 \times 1 \times 8$ supercells and meshes of $1 \times 3 \times 3$, $3 \times 1 \times 3$ and $3 \times 3 \times 1$ irreducible k-points were constructed, respectively. Convergence tests with larger k-point meshes were performed and the difference was found to be negligible. For example, the difference in decohesion energy of the V_2O_5 $3 \times 1 \times 1$ supercell (100) between k-point meshes of $1 \times 3 \times 3$ and $5 \times 5 \times 5$ was less than 1 %. For the tungsten trioxides, cleavage was considered in those planes where each structure bears a resemblance to the V_2O_5 (002) layer structure and thus the largest difference in metal–oxygen bonding distances. This is the (002) plane for WO_3 phases P 4/n c c Z, P 4/n m m Z, P $\bar{4}\,2_1$ m and P c n b and the (004) plane for the WO_3 phase P m n b. Accordingly, $1 \times 1 \times 4$, $1 \times 1 \times 8$, $1 \times 1 \times 8$, $1 \times 1 \times 4$ and $1 \times 1 \times 4$ supercells and k-point meshes of $5 \times 5 \times 1$ were constructed. In the cubic ReO_3 structure cleavage was carried out for the (100) plane, using a $8 \times 1 \times 1$ supercell and a $1 \times 5 \times 5$ k-point mesh.

2.2 Experimental methods

A common technique to grow thin films is by means of vapour deposition. Here, atoms, ions, molecules or clusters are precipitated at pressures much lower than the atmospheric pressure. There are “chemical vapour deposition” (CVD) techniques using molecular, gaseous precursors that react producing a solid phase, and “physical vapour deposition” (PVD) techniques using solid materials as the source, which is then evaporated, ablated or sputtered. Sputtering, in particular magnetron sputtering, is applied in this work. Based on the special set-up as described later in detail, the deposited thin films exhibit a gradient in chemical composition. To analyse the physical and chemical properties of the deposited thin films along the composition gradient, spatially resolved techniques are required.

2.2.1 Thin film deposition

During sputtering, a gas discharge plasma is maintained in a low pressure system. Typically noble gases such as argon at a pressure of 0.1 to 10 Pa are present. A notable share of charged particles, electrons and ions (such as Ar^{+}), is present at the discharge which can be controlled by electric and magnetic fields [163–165]. Momentum transfer by ions is utilised to sputter atoms from the source material, the so-called target. The target is fixed to the cathode and thus negatively charged, therefore positive ions from the process gas are accelerated towards its surface. Ion–surface interactions may result in recoil/reflection, implantation (at higher ion energies), secondary electron emission and sputtering [164, 166]. If these positive ions acquire an energy large enough to overcome the surface binding energy, atoms from the target are ejected and hence sputtering occurs. The sputtered atoms will eventually deposit on the surrounding surfaces including the substrate. For an illustration of a sputtering system and the two main mechanisms, ionisation of the process gas and sputtering atoms off the target, see Figure 2.2. For a more detailed introduction into the thin film deposition techniques applied here, the interested reader may be referred to more comprehensive literature [163–165, 167–169].

Sputter yield

The sputter efficiency or the sputter yield of a particle (here the argon ion) interacting with the target surface is dependent on several factors. The ion

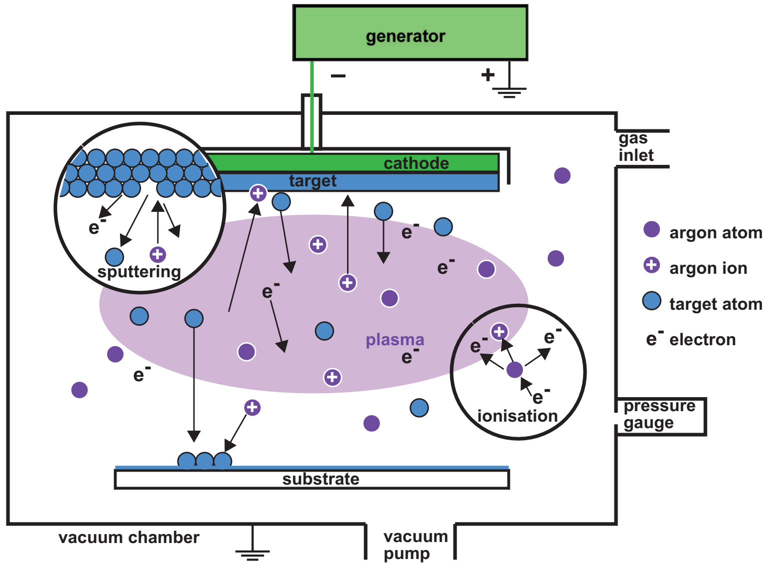

Figure 2.2: Schematic illustration of a sputtering system and main mechanisms (ionisation and sputtering).

energy E_i needs to exceed the target atom's binding energy $E_{B,t}$ to eject it from the surface. While the target potential U is affecting the ion energy, the binding energy is defined by the element and the respective target atom neighbours (so also on crystal orientations). Thus, there is a threshold energy/target potential to overcome, but a general correlation of the sputter yield Y and the voltage U applied at the target can be expressed as

$$Y \propto U^{1/2} [170]. \tag{2.9}$$

There are several theoretical and empirical formulation attempts, for further information see [168, 170–175]. For the collision itself, the momentum and energy transfer, the atomic numbers or ion masses of both the incident ion and the target atom need to be considered in addition to the above mentioned factors.

Sputtering techniques

The simplest sputtering system is a diode set-up where the target is the cathode and the grounded chamber acts as the anode. Diode sputtering can be carried out in direct current (DC) mode, pulsed DC mode or alternating current (AC) mode. Generally, non-conductive compound targets, e.g. oxides, require non-DC generators since necessary current flow cannot be initiated with DC. Common frequencies to sputter dielectric targets are the radio frequencies 13.56 and 27.12 MHz and therefore the term RF sputtering is used.

Substrate biasing

While the chamber itself is grounded and the current flow and thus the plasma can be sustained, the substrate may be grounded as well, floating or biased. A floating substrate has no potential applied and is thus charged up by the plasma (by electrons) until an equal flow of positive and negative particles is self-maintained as a steady state. During biasing, the substrate is kept at a constant (negative) voltage to attract ions bombarding the surface to cause densification and increase the adatom mobility (and hence better film quality even at lower deposition temperatures) [176, 177].

Reactive sputtering

The addition of other, non-noble and therefore reactive gases to the process gas during reactive sputtering leads to reactions between the sputtered metal and the respective gas to form compound films. Hence, oxygen can be added to grow oxide films and nitrogen to form nitrides. There are different reactive sputtering regimes with respect to the target surface condition:

- the metallic mode – the target condition is similar to non-reactive gas plasmas with the pure metal on the target surface,
- the poisoned mode or compound mode – the target consists of a compound made of the target material and the reactive gas and
- the transition zone in between, which undergoes a hysteresis loop for the reactive gas flow–pressure relation [178–180].

The actual target condition basically results from two competing processes: The sputtering of atoms from the target surface, and the covering of the target

surface with the reactive gas or rather the compound formed by the target material and the reactive gas [178, 181]. Both processes are foremost related to the reactive gas flow rate and the factors influencing its partial pressure, e.g. the pumping speed and the gettering by the sputtering material, the adsorption kinetics of the reactive gas on the target surface, its implantation and reaction with the target material, and the parameters determining the sputter rate, e.g. the cathode voltage and power/current (density), the secondary electron emission coefficient and the sputter yield [178, 180, 182, 183]. Due to the resulting interdependencies, a hysteresis arises for certain relations [178, 179, 182], e.g. for the before mentioned reactive gas flow–pressure relation. The sputter rate is significantly decreased for the poisoned mode compared to metallic mode operation (at the same average power) [179, 181]. This can be explained by the increased secondary electron emission [180, 181] and reactive gas implantation in the target [180].

Magnetron sputtering

To increase the sputter rate, magnetic fields are utilised to increase the ionisation probability in the target vicinity by increasing the electrons' trajectories. As a further advantage, process pressure can be significantly lower than for a simple diode system, increasing the mean free path of the particles. Probably the most common approach is magnetron sputtering (MS). Here, magnets behind the target are employed [169]. Though ionisation in the vicinity of the target is largely increased for the process gas, the metal ion fraction for direct current magnetron sputtering (DCMS) is with up to a few percent [184] rather small with respect to the total amount of the sputtered metal atoms.

High Power Pulsed Magnetron Sputtering

Since charged particles are easy to control with electromagnetic fields, an increased share of metal ions during sputtering can offer more options for tuning the energetics of the film forming species [185] and thus the film growth [186, 187]. Several approaches have been made to increase the fraction of metal ions, because such films are usually very dense and smooth [186, 187]. The ionisation of the sputtered flux also enables via structures to be densely filled [188]. One option is to use a pulsed DC-like approach but with extremely high power/current pulses, which is thus called High Power Pulsed Magnetron

Sputtering (HPPMS) or High Power Impulse Magnetron Sputtering (HiPIMS) [188, 189]. HPPMS utilises a much higher degree of ionisation of the sputtered flux, up to 40 to 70 % [188, 190], within plasma densities of $>10 \times 10^{13}$ cm^{-3} [190, 191]. The power densities for common DCMS processes are in the range of tens of W cm^{-2}, mostly limited by the cathode cooling, while a maximum value of 1000 W cm^{-2} was reported using a special cooling, enabling self-sputtering conditions [192]. Power density for HPPMS can be much higher than usual DCMS, up to 3 kW cm^{-2} peak power density [188, 191], while the average value is kept at moderate levels, allowing for the use of conventional cathode cooling.

If (positively charged) metal ions are present they will contribute to the sputtering in addition to the argon ions. The mechanism of metal ions sputtering the target is referred to as "self-sputtering" [193]. Consequently, the self-sputter yield needs to be larger than unity to sustain sputtering without feeding gas. The ability for self-sputtering depends to a large extent on the target material itself; the self-sputter yield, the ionisation energy and the secondary electron emission [193, 194].

Still, one drawback for the industrial application of HPPMS is the lower deposition rate compared to DCMS at the same time averaged power. For example, HPPMS deposition rates for Al, Al_2O_3 and TiO_2 depositions are typically reported to be about 25 to 35 % of the DCMS rate at the same time averaged power [193]. The physical reason for this behaviour could be explained by the non-linear energy dependence of the sputter yields [195]. The high power pulses lead to increased cathode current but also to a higher absolute value of the voltage, so according to the proportionality given in Equation 2.9 the yield cannot increase to the same extent as the power. Other reasons for the lower yield discussed are the "loss" of sputtered target ions, since some are accelerated back to the target causing the self-sputtering [193], a conductivity change in the plasma due to the metal ions and a lack of electrons [196] and the limitations in the transport to the substrate due to deflections of the metal ions by the magnetic field of the cathode [185, 197].

Combinatorial sputtering

Alloying or doping is straightforward when using sputtering techniques. Different film compositions can be obtained by sputtering a compound target (e.g. produced by sintering different metal powders) or simply applying multiple

targets/cathodes with different compositions. By using e.g. a two target set-up it is possible to vary the composition of the deposited film by the power applied to the targets or the positioning of the substrate relative to the targets. If the target is not rotated during the process, a composition gradient forms. This is intentionally used for combinatorial sputtering. With the use of this composition spread method, an efficient screening of different compositions/materials can be performed. Thus, a broad range of compositions within a material system's phase diagram can be covered in one deposition process, while conventional set-ups would require individual processes and maybe several compound targets for each film composition [27].

2.2.2 Experimental set-up for thin film depositions

The thin films were synthesised by reactive magnetron sputtering in a high vacuum system CC 800/9 HPPMS from CemeCon AG, Germany, with a base pressure of <0.05 mPa. DC and HPPMS techniques were used with a comparable time averaged power of 2.8 kW. The time averaged power density was 11.2 W cm^{-2}. For the DCMS deposition, Pinnacle Plus+ power supplies (Advanced Energy) were used in normal DC mode with a set cathode power. For the HPPMS deposition, Sinex 3.0 pulsed power supplies (Chemfilt Ionsputtering) were used with a cathode voltage of −750 V. The pulse width was set to 200 μs and the frequency to 400 Hz to ensure stable operation and high time averaged power. The target (500 mm $\times$ 88 mm) consisted of two segments; one sintered Ti-Al (50:50), the other pure W (Plansee Composite Materials GmbH), arranged in a way that a W composition gradient on the deposited films ranging from 10 to 52 at.% for DCMS and from 7 to 54 at.% for HPPMS was obtained. The argon flow was set to 150 sccm and 180 sccm nitrogen was added to maintain a total pressure of 600 mPa throughout the depositions. Polished single-crystal silicon wafers with a diameter of 50.8 mm were used as substrates. The nine wafers were clamped onto a stainless steel holder to cover the complete target length at a distance of 130 mm to the plasma source, as can be seen in Figure 2.3. Prior to deposition, the wafers were etched for 30 min by an argon plasma (200 mPa) with a 240 kHz pulsed DC voltage of −650 V applied to the sample holder. Substrates were heated from the back, reaching 420 °C at the surface. The substrate potential was set floating. Films were grown for one hour.

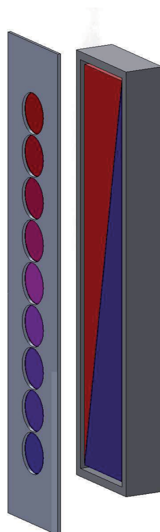

Figure 2.3: Schematic illustration of the synthesis strategy. The colour gradient of the substrates indicates the composition gradient.

Cathode voltage and current characteristics

Cathode voltage and current were recorded during HPPMS depositions using appropriate converters with an oscilloscope. Average and peak values are given in Table 2.1, and the average over 128 cycles of the time dependent voltage and current traces is shown in Figure 2.4. As can be seen, the cathode voltage surpasses the set-point of −750 V and then drops rapidly to about −450 V as the current is increased. The cathode current rises and falls in a parabolic way and reaches its peak 35 µs after the voltage. The peak current indicates the inflexion point of the voltage curve. The effective pulse length of about 80 µs is restricted by the power supply's capacitors.

Table 2.1: TiAlN–WN$_x$ deposition conditions for DCMS and HPPMS. For DCMS, the given values are constant and for HPPMS, the given values present time averaged and peak values. The set values for the HPPMS power supply were −750 V for voltage, 200 µs pulse width and 400 Hz repetition rate.

		DCMS	HPPMS
(time averaged) power	(kW)	2.8	2.8
(peak) power	(kW)	2.8	160
(peak) voltage	(V)	−435	−850
(peak) current	(A)	6.5	230
(time averaged) current	(A)	6.5	4.2
(peak) current density	(mA/cm^2)	15	520
(peak) power density	(W/cm^2)	6.4	365

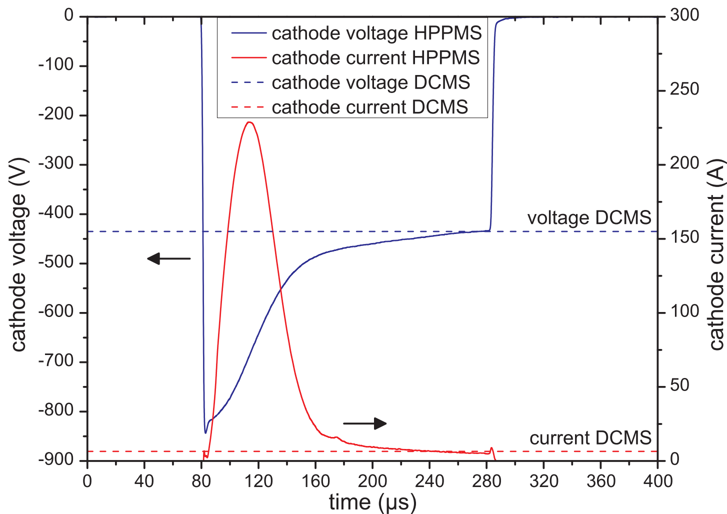

Figure 2.4: Cathode voltage (blue) and current (red) during deposition of TiAlN–WN$_x$ using DCMS (dashed lines) and HPPMS (full lines). The set values for the HPPMS power supply were −750 V, 200 µs and 400 Hz, resulting in a time averaged power of 2.8 kW. DCMS power was set to the same value.

2.2.3 Scanning electron microscopy

Scanning electron microscopy (SEM) allows for imaging beyond the resolution and depth of field of white light optical microscopes [198, 199]. A schematic illustration of an SEM is shown in Figure 2.5. An electron beam produced by a hot filament cathode or field emission (FE) gun (the latter one will give a more coherent beam with higher current density and thus result in better resolution and image quality) is accelerated to several keV and focussed on the sample surface.

Interaction of the incident beam and the surface atoms of the sample leads to electron emission, which can be measured with an electron detector. Although the beam diameter is in the order of 1 nm, the lateral resolution is worse because the interaction volume of the electrons and hence the area of electron emission inside the material is larger than the beam diameter. The interaction volume is pear-shaped and the penetration depth is depending on the acceleration voltage/electron energy (in the kV range) as well as on the atomic number and sample density, for metals usually in the order of µm.

The main electron-emitting interactions are the emission of secondary electrons and backscattering of electrons. Both types of emission can be differentiated by their specific energy range so that distinct secondary electron images (SEI) and those of backscattered electrons (BSE) can be taken. To minimise interactions of the electrons with the atmosphere, SEM devices operate at high vacuum. The secondary electrons are emitted by inelastic scattering of the incident beam electrons at the surface atoms. Their energy is in the eV range, so detected electrons originate from the first few nm of the sample material (for most inorganic materials). Therefore, SEI enables high resolution images of the sample topography and is the most common SEM mode. Image contrast results from the detected electron current, which is dependent on the way the electrons need to escape the material and thus the surface morphology. BSE are elastically scattered electrons from the incident beam which are reflected out of the sample and hence have very high energy. Depending on the acceleration voltage, penetration depth and thus depth of information is up to some µm and thus resolution is worse than for SEI. Since heavy elements cause stronger backscattering than lighter elements, some information about the elemental distribution can be obtained.

To obtain a two-dimensional image of the sample, the surface is scanned with the electron beam so that the intensity of the detected signal can be

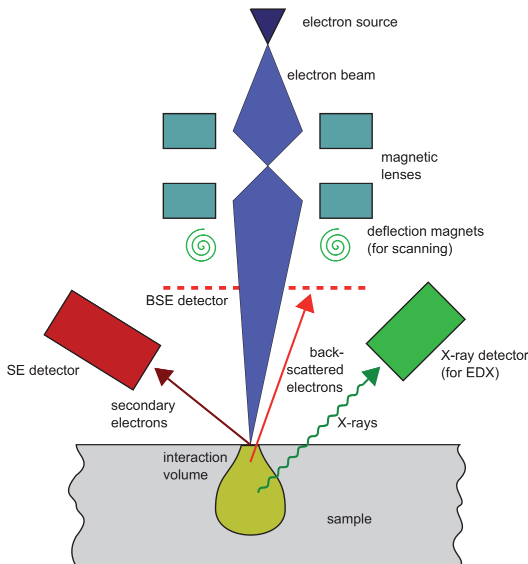

Figure 2.5: Schematic illustration of a scanning electron microscope (SEM) with an integrated energy-dispersive X-ray spectroscope (EDX).

displayed depending on the beam's position. Samples for SEM should be electrically conductive, otherwise the surface is charged by the electron beam and artefacts will be measured. Hence, non-conductive samples are usually coated with a thin conductive layer (e.g. carbon or gold).

For this work, a Jeol JAMP-9500F Auger-Microprobe with a field emission scanning electron microscope (FE-SEM) was used to analyse the film morphology by taking cross-section SEM (X-SEM) images using secondary electrons.

2.2.4 Energy-dispersive X-ray spectroscopy

When taking an SEM image, not only secondary or backscattered electrons but also X-rays are emitted from the sample surface [199]. When the electron beam ejects an inner shell electron, a higher energy electron from an outer shell fills the hole. The energy difference between the two electron levels is released as an X-ray photon. Due to the discrete nature of the energy levels for each element, the emitted X-rays have a certain energy. Thus, the emitted X-rays or X-ray spectra are characteristic for each element and can therefore

be analysed by energy-dispersive X-ray spectroscopy (EDX or EDS) or wavelength dispersive X-ray spectroscopy (WDX or WDS) to obtain the elemental composition of the probed sample. While EDX allows simultaneous detection of different elements and is thus a relatively fast method, a WDX detector can only measure one element at once but has higher sensitivity and gives higher lateral resolution. The depth of information is depending on the acceleration voltage of the electron beam and thus the electrons' penetration into the material. Therefore, acceleration voltage should be low enough to avoid interaction with the sample substrate. However, it needs to be high enough to enable X-ray emission of the elements to be detected, which can be calculated based on the energies of the specific electron shells. Therefore, acceleration voltage for EDX is usually several times higher than for normal SEM. In order to quantitatively analyse the elemental composition of the probed sample, an appropriate standard should be used for calibration, especially if the sample contains light elements (i.e. for oxides, nitrides). The accuracy of the EDX measurements is usually about $\pm$1–2 at.% [199]. The uncertainty is expected to be higher for the light elements, especially nitrogen.

Here, composition of the deposited films was determined by EDX carried out with an EDAX Genesis 2000 in a Jeol JSM 6480 scanning electron microscope. The acceleration voltage was 10 kV. A $Ti_{0.30}Al_{0.23}W_{0.37}N$ standard sample analysed by WDX was used.

2.2.5 X-ray diffraction

For structural investigations of thin films, X-ray diffraction (XRD) [200, 201] is a widely used characterisation method. Incident X-rays with a wavelength λ in the magnitude of the material's interplanar spacing are scattered in the material according to it's crystallographic structure. Interactions take place between the X-ray waves and the electron shells of the periodically arranged atoms. The intensity of the scattered beam is measured in dependence of the angle θ between incident beam, sample surface and diffracted beam, see Figure 2.6. Depending on the interplanar distances d of the crystallographic planes, diffraction occurs. Hence, high intensity of the emergent beam can be detected in case of constructive interference when the path difference between two scattered waves is equal to λ or an integer multiple $n\lambda$. Bragg diffraction is schematically drawn in Figure 2.6.

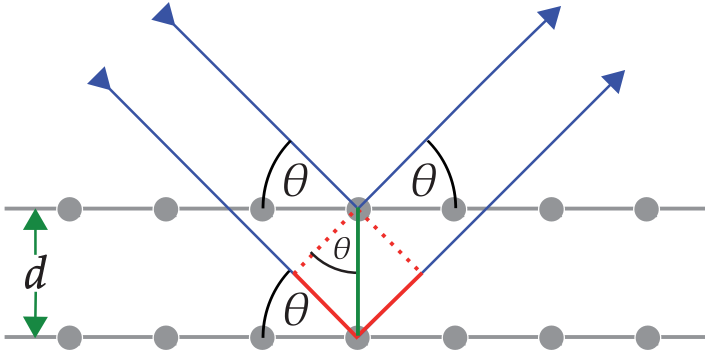

Figure 2.6: Schematic illustration of the Bragg diffraction. The X-rays (illustrated as blue lines) with an incident angle θ are scattered at the grey atoms of a certain crystal plane with the interplanar spacing d. The resulting path difference $2d\sin\theta$ is marked as red lines.

According to Bragg's law,

$$2d\sin\theta = n\lambda, \tag{2.10}$$

the correlation between the diffraction angle θ and the interplanar distance d can be calculated. The lattice parameter a can be calculated from d for a given crystal symmetry. In the case of cubic crystal structures, as for TiN, the correlation between a and d for the plane set (hkl) is

$$d = \frac{a}{\sqrt{h^2 + k^2 + l^2}}. \tag{2.11}$$

Thus, scanning a θ range will give the diffraction pattern or diffractogram of the measured crystalline material. For a certain phase, the diffraction pattern will be unique due to its distinct interplanar distances in combination with its crystal structure/symmetry. Therefore, XRD can be used for phase identification by comparing the position and intensity of the measured data with known phase data, e.g. from an appropriate database like the *Powder Diffraction File* (PDF) maintained from the Joint Committee on Powder Diffraction Standards and the International Centre for Diffraction Data (JCPDS-ICCD).

The here investigated thin films are generally of polycrystalline nature and the X-ray beam will be scattered at much more than one grain as the penetration volume is significantly larger than the average grain size. Therefore,

for a given incidence angle ω of the X-ray beam, more than one diffraction condition according to Bragg's law in Equation 2.10 is fulfilled due to various grain orientations and different $d/(hkl)$ sets per phase. Scanning a 2θ range will give the diffraction pattern of the measured polycrystalline sample (or powder).

For this work, structural investigation by XRD was conducted in a Bruker AXS D8 Discover General Area Detection Diffraction System with Cu-K_α radiation. The generator settings were 40 kV and 40 mA for voltage and current, respectively. A collimator with a diameter of 0.5 mm and an incidence angle ω of 15° were used, resulting in an elliptical surface area segment diffraction of 0.64 mm × 2.47 mm. The probed 2θ range was 25 to 115°. The lattice parameter was obtained from the (111) and (200) peaks.

2.2.6 Nanoindentation

Hardness is commonly measured by indenting the material with a harder counterpart of a known geometry. The indentation area or depth/displacement is analysed with respect to the indenter tip geometry and indentation load. Over time, several techniques for indentation hardness measurement have been developed, mainly differing in the tip geometry. For hardness measurements on thin films, indentation depth should be less than 1/10 of the film thickness to avoid influence of the substrate on the plastic deformation zone [202]. Hence, such sensitive and small-scaled hardness analysis is referred to as nanoindentation (NI). One common tip is the Berkovich diamond tip, a relatively flat three-sided pyramid shape with a total included angle of 142.3° [203].

Since normal optical analysis of indents in the sub-µm region is not convenient, a prerequisite for NI is that the load P and the resulting displacement h of the tip is measured simultaneously during the indentation. Knowing the exact tip shape, the indentation area A can be calculated from the indentation depth h (by the so-called tip area function) [202, 204]. An exemplary load–displacement curve is shown in Figure 2.7.

Hardness is calculated from the relation of the maximum applied indentation load P_{max} and the indentation area A:

$$H = \frac{P_{max}}{A}. \tag{2.12}$$

The residual indentation area is calculated from the contact depth h_c, the depth at which the contact between the tip and the sample is made, h_{max} excluding

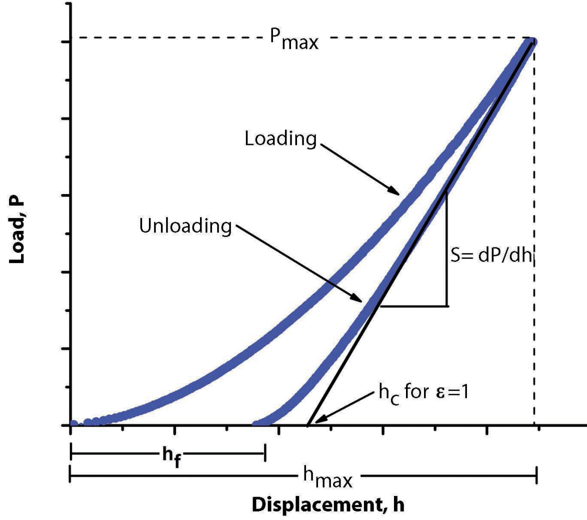

Figure 2.7: Schematic load–displacement curve [205]. The indentation is carried out up to the maximum load P_{max} with the corresponding displacement h_{max}. After unloading, the remaining depth of the contact impression is h_f.

the non-contact, elastic deformation around the indentation/contact area. For the geometry of a Berkovich tip, the area can be approximated as $A \approx 24.5\, h_c{}^2$.

Since load P and resulting displacement h of the tip is measured simultaneously during the indentation, elasticity data like Young's modulus E can be obtained from the load–displacement curve as shown in Figure 2.7. The measured stiffness of the contact,

$$S = \frac{dP}{dh}, \tag{2.13}$$

is retrieved from the slope of the unloading curve, usually the region between 95 % and 20 % of the loaded force [204]. However, this includes both the probed sample and the indentation device, so only the reduced elastic modulus E_r can be calculated as

$$E_r = \frac{\sqrt{\pi}}{2} \frac{S}{\sqrt{A(h_c)}}. \tag{2.14}$$

Young's modulus E can be calculated from E_r knowing the Poisson's ratio ν of the probed material and the elastic behaviour of the machine incl. the tip (indexed i):

$$\frac{1}{E_r} = \frac{1-\nu^2}{E} + \frac{1-\nu_i{}^2}{E_i} \tag{2.15}$$

Care needs to be taken for the sample preparation and mounting to avoid influence to the measurement, also sample roughness should be very low.

Within this work, NI experiments were performed in a Hysitron TriboIndenter coupled with an atomic force microscope. A Berkovich diamond tip, with the tip area function and machine compliance obtained from calibration on fused silica, was applied for the measurements using the Oliver and Pharr method [204]. Sapphire was used as a second reference material. Samples were characterised by 15 indents each for a load of 5000 µN. The contact depth was about 65 nm and thus less than 10 % of the film thickness of 1.8 to 3.2 µm, neglecting a possible influence of the substrate. To determine the elastic modulus from the load displacement data, the Poisson's ratio was assumed to be 0.25.

3 Results and discussion

3.1 *Ab initio* calculation of vanadium oxides

To understand the correlation between composition, structure, elastic and mechanical properties of vanadium oxides, *ab initio* calculations have been applied as described in Chapter 2.1.2 to obtain the structural data, the bulk modulus, the elastic constant C_{44} (as a measure of the shear modulus) [148, 149], the decohesion energies and the electron density distribution for seven different vanadium oxides VO_x ($1 \leq x \leq 2.5$) with vanadium valency from 2 to 5, including mixed-valency phases and phases of the V_nO_{2n+1} homologous series.

3.1.1 Crystal structure

The calculated structural data of the different phases – formula, space group, lattice parameters, volume (per atom) and number of formula units per unit cell (Z) – as well as fractional atomic coordinates and Wyckoff positions have been calculated and are presented for VO (rock salt structure, F m$\overline{3}$m) in Table 3.1, V_2O_3 (karelianite structure, the vanadium counterpart of corundum, R $\overline{3}$c) in Table 3.2, VO_2 (rutile structure, P 4_2/m n m) in Table 3.3, V_6O_{13} (C m m a) in Table 3.4, V_4O_9 (P n m a) in Table 3.5, V_3O_7 (I 4/m m m) in Table 3.6 and V_2O_5 (shcherbinaite, P m m n) in Table 3.7.

VO, Table 3.1, exhibits rock salt structure with a calculated lattice parameter a = 4.186 Å for an ideal, stoichiometric crystal without defects. This is slightly larger than the experimental value of 4.12 Å [130], resulting in a vol-

Table 3.1: VO cell description.

formula	VO
space group	F m$\overline{3}$m (225)
a (Å)	4.186
V (Å^3 atom^{-1})	9.169
Z	4

atom	site	x	y	z
V	4 b	0.0	0.0	0.0
O	4 a	0.5	0.5	0.5

Table 3.2: V_2O_3 cell description with hexagonal axes.

formula	V_2O_3
space group	R $\bar{3}$ c (167) (hexagonal axes)
a (Å)	4.925
c (Å)	13.834
V (Å^3 atom^{-1})	9.687
Z	6

atom	site	x	y	z
V	12 c	0.0	0.0	0.341
O	18 e	0.329	0.0	0.25

Table 3.3: VO_2 cell description.

formula	VO_2
space group	P 4_2/m n m (136)
a (Å)	4.558
c (Å)	2.858
V (Å^3 atom^{-1})	9.897
Z	2

atom	site	x	y	z
V	2 a	0.0	0.0	0.0
O	4 f	0.300	0.300	0.0

Table 3.4: V_6O_{13} cell description.

formula	V_6O_{13}
space group	C m m a (67)
a (Å)	11.935
b (Å)	19.940
c (Å)	3.687
V (Å^3 atom^{-1})	11.545
Z	4

atom	site	x	y	z
V	16 o	0.147	0.069	0.75
V	8 n	0.148	0.25	0.75
O	16 o	0.174	0.049	0.25
O	16 o	0.151	0.153	0.75
O	8 n	0.177	0.25	0.25
O	8 m	0.0	0.056	0.75
O	4 g	0.0	0.25	0.75

Table 3.5: V_4O_9 cell description.

formula	V_4O_9
space group	P n m a (62)
a (Å)	17.910
b (Å)	3.642
c (Å)	9.452
V (Å^3 atom^{-1})	11.858
Z	4

atom	site	x	y	z
V	4 c	0.491	0.25	0.274
V	4 c	0.080	0.25	0.543
V	4 c	0.163	0.25	0.205
V	4 c	0.313	0.25	0.449
O	4 c	0.024	0.25	0.727
O	4 c	0.449	0.25	0.049
O	4 c	0.339	0.25	0.654
O	4 c	0.198	0.25	0.005
O	4 c	0.088	0.25	0.341
O	4 c	0.047	0.25	0.088
O	4 c	0.392	0.25	0.357
O	4 c	0.167	0.25	0.584
O	4 c	0.240	0.25	0.316

Table 3.6: V_3O_7 cell description.

formula	V_3O_7
space group	I 4/m m m (139)
a (Å)	13.986
c (Å)	3.631
V (Å^3 atom^{-1})	11.838
Z	6

atom	site	x	y	z
V	2 a	0.0	0.0	0.0
V	8 h	0.184	0.184	0.0
V	8 i	0.366	0.0	0.0
O	2 b	0.0	0.0	0.5
O	8 h	0.099	0.099	0.0
O	8 h	0.294	0.294	0.0
O	8 j	0.094	0.5	0.0
O	16 l	0.290	0.093	0.0

Table 3.7: V_2O_5 cell description.

formula	V_2O_5
space group	P m m n (59)
a (Å)	11.532
b (Å)	3.600
c (Å)	4.401
V (Å^3 atom^{-1})	13.051
Z	2

atom	site	x	y	z
V	4 f	0.102	0.25	0.890
O	4 f	0.106	0.25	0.523
O	4 f	0.931	0.25	0.003
O	2 a	0.25	0.25	0.004

ume difference of 4.9 %. Since VO is defect stabilised and exhibits vacancy concentrations of approximately 15 % for both metallic and oxygen sites [206], this deviation seems reasonable. All other vanadium oxides considered, i.e. V_2O_3 (Table 3.2), VO_2 (Table 3.3), V_6O_{13} (Table 3.4), V_4O_9 (Table 3.5), V_3O_7 (Table 3.6) and V_2O_5 (Table 3.7), exhibit better agreement with previously published structural data [125–129, 131]. The deviations between the calculated and measured lattice parameter values are within 0.1 to 1.2 %, except for V_3O_7 where c differs by 2.5 %, resulting in a volume difference of 0.4 to 2.8 %.

3.1.2 Energy of formation

Information about phase stability is obtained from energy of formation E_f, given in Table 3.8. For all calculated phases the energy of formation with respect to the elements is negative. However, for VO E_f with respect to the elements is −1.778 eV atom^{-1} and therefore much higher than for the other phases, which are within the range of −2.635 to −2.794 eV atom^{-1}. For the ideal, defect-free stoichiometric VO (rock salt structure), as described here, E_f lies clearly above the ground-state convex hull of the energy–composition diagram, suggesting decomposition in the neighbouring, stable phases V and V_2O_3. Defect-stabilised rock salt structured VO_x $(0.8 \leq x \leq 1.3)$ was considered previously [206–208]. A stable stoichiometric phase has been reported with a vacancy concentration of approximately 15 % at metal and oxygen sites [206]. DFT-based calculations on the stability of vanadium oxide growing on metal surfaces have been carried out by Kresse *et al.* [112]. It was shown that a stoichiometric VO defect structure with a 25 % metal and oxygen vacancy concentration is stable with respect to V and V_2O_3. Since these defects are not within the scope of this study, further discussion on VO will be omitted due to its apparent structural instability. For V_4O_9, the energy of formation is −2.766 eV atom^{-1} and hence above both E_f (V_6O_{13}) =−2.794 eV atom^{-1} and E_f (V_3O_7) = −2.773 eV atom^{-1}. It therefore lies slightly above the ground-state convex hull of the energy–composition diagram, suggesting decomposition in the neighbouring phases V_6O_{13} and V_3O_7.

3.1.3 Elastic properties

Table 3.8 contains the calculated properties of VO, V_2O_3, VO_2, V_6O_{13}, V_4O_9, V_3O_7 and V_2O_5. The data provided are vanadium valency, oxygen content

in the phases, energy of formation E_f, volume, bulk modulus B, elastic constant C_{44} and B/C_{44}. The elastic data are given for

(i) uniform compression (single relaxation at equilibrium) and

(ii) with full structural relaxation at every volume.

C_{44} is used as a measure of the shear modulus and the B/C_{44} ratio may be interpreted as a measure of plasticity [148, 149].

In all discussions below, B and C_{44} data for full structural relaxation for every volume are considered. These values are shown in Figure 3.1 as a function of vanadium valency. As the V valency is increased from 3 to 5, B decreases by 61 % from 222 to 87 GPa. For V_nO_{2n+1} series phases V_6O_{13} and V_3O_7, B is approximately 160 GPa. However, for V_4O_9 B is 104 GPa. This relatively low value in relaxed mode (ii) and the corresponding energy–volume curve (not shown here) may indicate a possible phase transformation. Also, according to the E_f data, V_4O_9 is unstable with respect to its neighbouring phases V_6O_{13} and V_3O_7. Hence, further discussion of this phase is omitted. Structural prototypes of V_2O_3 and VO_2 are corundum (α-Al_2O_3) and rutile (TiO_2), respectively. For corundum and rutile, the calculated B values are 232 and 213 GPa, differing by 4.5 and 6.2 % from the vanadium oxide counterparts, respectively. Experimental data of 246 GPa for corundum [209] and 212 GPa for rutile [210] are consistent with the calculations. As the valency of vanadium is increased from 3 to 5, the C_{44} values decrease by 83 % from 153 to 25 GPa. V_2O_3 and VO_2 exhibit, with 153 and 128 GPa, C_{44} values similar to their prototypes, corundum (133 GPa calculated here, 147 GPa experimental [209]) and rutile (127 GPa calculated here, 124 GPa experimental [210]), respectively. However, as the V valency is increased to > 4 for V_6O_{13} and V_3O_7, C_{44} significantly decreases to 76 and 63 GPa, respectively, and drops down to 25 GPa for V_2O_5. Thus, these phases constitute easily plastically deformable structures, despite comparatively large bulk moduli. The calculated C_{44} value of −89 GPa for defect-free, stoichiometric VO is negative, suggesting structural instability [151], which is consistent with the discussion above.

The B/C_{44} ratio for the vanadates discussed here (except VO and V_4O_9) are shown in Figure 3.2 as a function of vanadium valency. Experimental values for diamond, known solid lubricants such as silver and gold [211], as well as calculated values for MAX phase nanolaminates Ti_3SiC_2 [212] and Y_2AlC [213] are included for comparison. As the V valency is increased from 3 to 5, the

Table 3.8: Calculated properties of the vanadium oxides VO, V_2O_3, VO_2, V_6O_{13}, V_4O_9, V_3O_7 and V_2O_5. The table presents vanadium valency, oxygen content and energy of formation E_f for each phase as well as volume per atom V, bulk modulus B, elastic constant C_{44} and B/C_{44} ratio. Elastic data are given for (i) uniform compression and (ii) with full structural relaxations at every volume.

		VO	V_2O_3	VO_2	V_6O_{13}	V_4O_9	V_3O_7	V_2O_5
valency		2	3	4	4.333	4.5	4.667	5
oxygen content		0.5	0.6	0.667	0.684	0.692	0.7	0.714
E_f (eV atom^{-1})		−1.778	−2.636	−2.770	−2.794	−2.766	−2.773	−2.733
V (Å^3 atom^{-1})		9.169	9.687	9.897	11.545	11.858	11.838	13.051
(i)	B (GPa)	243.6	253.8	248.5	208.1	197.3	202.3	173.5
	C_{44} (GPa)	−88.6	165.2	155.1	74.7	78.6	75.5	40.2
	B/C_{44}		1.54	1.60	2.79	2.51	2.68	4.32
(ii)	B (GPa)	243.6	221.7	226.6	166.7	103.7	158.0	86.6
	C_{44} (GPa)	−88.6	153.3	127.8	75.9	66.3	63.2	25.3
	B/C_{44}		1.45	1.77	2.20	1.57	2.50	3.42

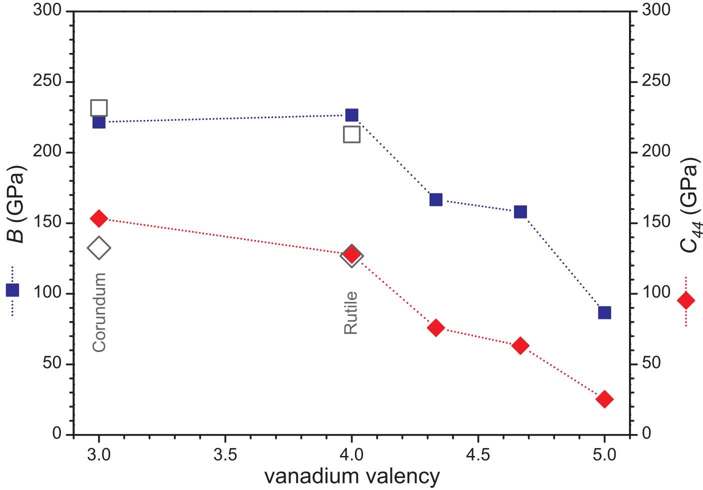

Figure 3.1: Bulk modulus B (squares/blue) and elastic constant C_{44} (diamonds/red) as a function of vanadium valency. Corundum and rutile are included for comparison and shown in open symbols.

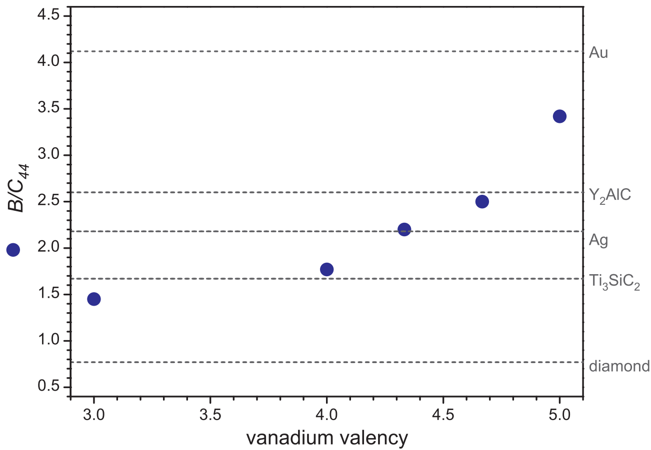

Figure 3.2: B/C_{44} ratio as a function of vanadium valency. Experimental values for diamond, silver and gold [211] as well as calculated values for MAX phase nanolaminates Ti_3SiC_2 [212] and Y_2AlC [213] are shown as dashed lines for comparison.

B/C_{44} ratio increases by a factor of 2.4 from 1.4 to 3.4. V_2O_3 and VO_2 exhibit B/C_{44} ratios of 1.4 and 1.8, respectively. According to the data provided in Figure 3.1, these ratios are similar to those of their prototypes corundum and rutile, which are not included in Figure 3.2. For V_6O_{13} and V_3O_7, B/C_{44} ratios of 2.2 and 2.5, respectively, are larger than for solid lubricant silver and Ti_3SiC_2. The largest B/C_{44} ratio is obtained for V_2O_5 with 3.4, approaching the ratio for gold. Due to their large B/C_{44} ratios, these oxides are expected to possess lubricating properties.

3.1.4 Decohesion energies

In order to identify possible shear planes for VO_2 and V_2O_5, decohesion energies for cleavage G were calculated for {100} and {200} planes in each independent lattice direction (see Table 3.9). These phases are chosen because they exhibit a large difference in B/C_{44}. Due to the VO_2 symmetry, $P4_2/mnm$, cleaving in (100), (200), (010) and (020) planes yields identical results, $G = 4.57\ \mathrm{J\,m^{-2}}$, while cleaving in (001) and (002) planes gives $2.15\ \mathrm{J\,m^{-2}}$. For V_2O_5, Pmmn, cleaving in (100) and (200) planes results in 0.69 and $0.70\ \mathrm{J\,m^{-2}}$, respectively. Within the accuracy of these calculations, the latter two values can be considered identical as expected due to symmetry. For cleaving in the equivalent (010) and (020) planes, $G = 1.21\ \mathrm{J\,m^{-2}}$ is obtained. Cleaving V_2O_5 in (001) and (002) planes results in a decohesion energy of 4.06 and $0.05\ \mathrm{J\,m^{-2}}$, respectively. Obviously, there is a large anisotropy in decohesion energies, especially in the case of V_2O_5, for which the spread is over two orders of magnitude. The decohesion energies calculated here for V_2O_5 are consistent with the surface energy data obtained previously [116]. The lowest decohesion energies in each direction for VO_2 and V_2O_5 are presented in Figure 3.3. For comparison, decohesion energy for the basal plane of MAX phases Ti_2AlC and Cr_2AlC [214] as well as for the (100) and the (110) plane of NiAl [162] are included. V_2O_5 shows an anisotropic behaviour with the value for the

Table 3.9: Decohesion energies for cleavage of {100} and {200} planes in VO_2 and V_2O_5.

structure	VO_2		V_2O_5			
plane	{100} {200}	{001} {002}	{100} {200}	{010} {020}	{001}	{002}
G ($\mathrm{J\,m^{-2}}$)	4.57	2.15	0.69	1.21	4.06	0.05

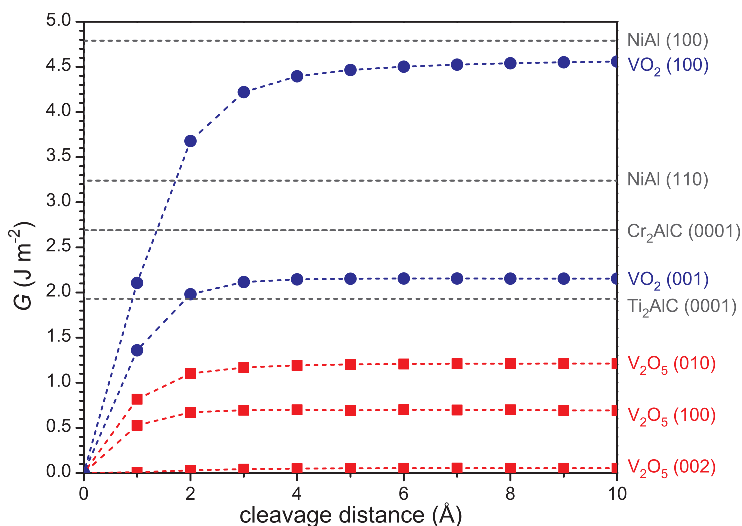

Figure 3.3: Decohesion energy G as a function of the distance between the cleaved blocks. Circles (blue) present VO_2, squares (red) V_2O_5. MAX phases Ti_2AlC and Cr_2AlC [214] as well as NiAl [162] are included for comparison.

V_2O_5 (002) plane cleavage being extremely low. It is only 2.8, 2.0 and 1.6 % of the decohesion energies for Ti_2AlC (0001), Cr_2AlC (0001) and NiAl (110), respectively. This very low decohesion energy is comparable with the surface energy of graphite (0.08 J m^{-2}) [159]. Furthermore, these data are consistent with the B/C_{44} ratios presented above. Thus, it can be expected that this easy cleaving plane enables plastic deformation and is therefore responsible for the vanadium pentoxide's lubricating properties.

These decohesion energies can be related to the (original) distance between the cleaved crystal layers, as shown in Figure 3.4. Short layer distance results in high decohesion energy, as seen for VO_2 where distances of 1.14 and 1.43 Å result in decohesion energies of 4.57 and 2.15 J m^{-2}, respectively. Accordingly, large distance results in low decohesion energy, as can be seen for the V_2O_5 (002) plane with a distance of 2.83 Å resulting in a decohesion energy of 0.05 J m^{-2}. These data suggest that the bonding distance between the cleaved layers is one of the key factors determining the decohesion energy for the phases studied here.

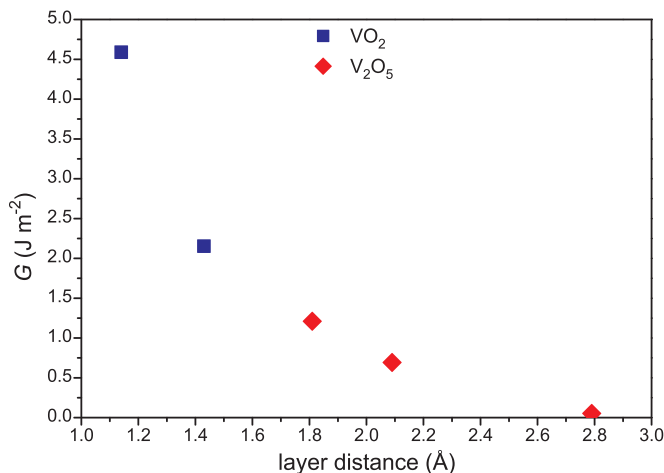

Figure 3.4: Decohesion energy as a function of the layer distance for the {200} planes of VO_2 (squares/blue) and V_2O_5 (diamonds/red).

3.1.5 Electron density distribution

The elastic properties and decohesion energies of these vanadium oxides may be understood based on the electronic structure. Electron density distribution obtained by the *ab initio* calculations are presented for V_2O_3 and VO_2 in Figure 3.5 and V_6O_{13}, V_3O_7 and V_2O_5 in Figure 3.6. In general, these oxides may be characterised by ionic bonding, due to the charge transfer from vanadium to oxygen. To some extent, there is charge shared between these two elements, giving rise to smaller covalent contribution. In particular for the V_2O_5 vanadyl bond, covalent character is apparent. It is important to note that these EDDs never exhibit regions without charge ($0\,\mathrm{eV\,Å^{-3}}$), which may indicate that some minor metallic contributions are present. However, striking differences between these phases can be observed. In V_2O_3 and especially in VO_2 (Figure 3.5), there are only very small regions with low electron density between the ions, or rather between the V–O polyhedra. This in turn may imply relatively strong bonding. Ionic structures, such as NaCl, are strongly bonded because of the large charge difference and the short distance between neighbouring atoms. For V_6O_{13}, V_3O_7 and especially V_2O_5 (Figure 3.6), there are very large regions with low electron density. In particular, two distinctive regions within the EDDs can be identified:

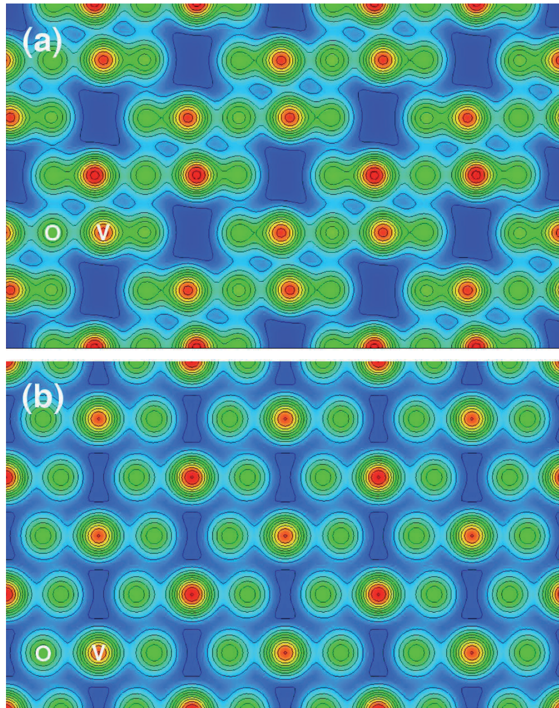

Figure 3.5: Electron density distribution of **(a)** V_2O_3 projected along the [100] axis (1 × 2 supercell); **(b)** VO_2 projected along the [100] axis (3 × 3 supercell). The EDD increases from 0.0034 to 2.159 and from 0.0047 to 2.141 a.u., respectively. Within this ionic structure, there is a minor contribution from covalent and metallic bond character, since a non-negligible electron density between the ions can be seen. No distinct shear planes are identifiable.

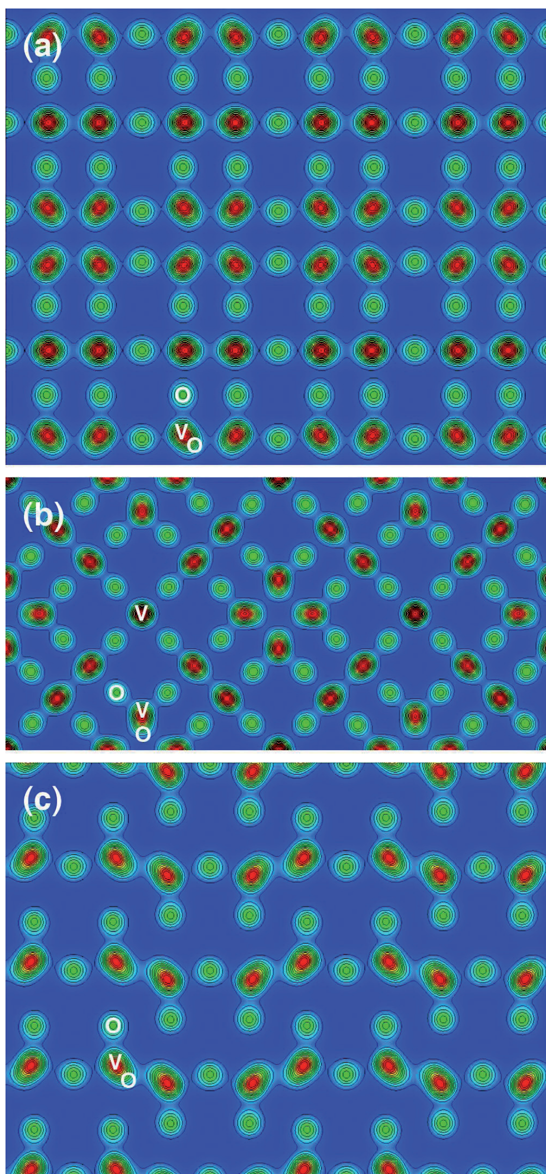

Figure 3.6: Electron density distribution of **(a)** V_6O_{13} projected along the [001] axis (2 × 1 supercell); **(b)** V_3O_7 projected along the [001] axis (2 × 1 supercell); **(c)** V_2O_5 projected along the [010] axis (2 × 4 supercell). The EDD increases from 0.0003 to 2.139 , 2.134 and 2.131 a.u., respectively.

(i) regions with high electron density and

(ii) regions with low electron density.

The high electron density regions may be assigned to V–O polyhedra, separated by the low electron density regions between the V–O polyhedra, or rather between the layers. Thus, only weak ionic bonding between the layers is established. Upon insertion of free electrons, as argued above, the Coulomb potential may be screened so that an exponential term should be added [211]. I suggest that the screened Coulomb potential and the presence of large low electron density regions in V_6O_{13}, V_4O_9, V_3O_7 and V_2O_5 are responsible for the low C_{44} values and therefore enable easy plastic deformation.

3.1.6 Conclusions

Different vanadium oxide phases ranging from V valency 2 to 5, including VO, V_2O_3, VO_2, V_6O_{13}, V_4O_9, V_3O_7 and V_2O_5, have been investigated in terms of bulk modulus and elastic constant C_{44} using *ab initio* calculations. As the V valency is increased from 3 to 5, C_{44} decreases from 153 to 25 GPa, whereas the bulk modulus values decrease from 222 to 87 GPa. Vanadium(III) and vanadium(IV) oxide have similar bulk moduli and C_{44} values as their structural prototypes corundum and rutile. The most promising properties in terms of solid lubrication, e.g. for protective coatings in metal cutting applications, are observed for vanadium pentoxide. In this phase, vanadium is in its highest oxidation state. When oxidising vanadium from V_2O_3 to V_2O_5, the V valency induced change in the crystal and bonding structure causes the B/C_{44} ratio to increase from 1.4 to 3.4. This is consistent with calculated decohesion energies of VO_2 and V_2O_5. The lowest decohesion energy for VO_2 is 2.15 J m^{-2}, whereas for V_2O_5 it is 0.05 J m^{-2}, being extremely low in comparison to other cleavage directions in the same structure and that by at least a factor of 10. This very low decohesion energy is similar to calculated surface energy for graphite (0001) (0.08 J m^{-2}) [159]. The bonding of phases exhibiting high C_{44} values is predominantly ionic with some minor contributions of covalent and metallic character. Due to the screened Coulomb potential between the layers in the phases exhibiting low C_{44} values, such as V_6O_{13}, V_4O_9, V_3O_7 and V_2O_5, the bond strength decreases rapidly as the distance is increased, resulting in weak coupling between the layers which then causes the formation of easily plastically deformable structures.

3.2 *Ab initio* calculation of Magnéli phase oxides

In the previous Chapter 3.1, it has been shown for VO_2 and V_2O_5 that the calculated decohesion energies were inversely proportional to the original distance between the cleaved layers. This behaviour could be described to be dependent on the screened Coulomb potential between the layers. For a further understanding of the correlation between the (electronic) structure and the elasticity as well as the decohesion energies of Magnéli phase oxides, studies have been extended to five WO_3 phases, a WO_3 parent structure ReO_3, MoO_2 and TiO_2 (rutile), which are compared to VO_2 and V_2O_5. Hence, the crystallographic structure, the bulk modulus, the elastic constant C_{44}, the decohesion energies and the electron density distribution have been obtained.

3.2.1 Crystal structure

The calculated structural data of the different phases – formula, space group, lattice parameters, volume (per atom) and number of formula units per unit cell (Z) – as well as fractional atomic coordinates and Wyckoff positions, have been calculated and are presented for five phases WO_3, namely WO_3 (P 4/n c c Z structure) in Table 3.10, WO_3 (P 4/n m m Z) in Table 3.11, WO_3 (P $\bar{4}2_1$ m) in Table 3.12, WO_3 (P c n b) in Table 3.13 and WO_3 (P m n b) in Table 3.14. In addition, data is given for a WO_3 parent structure ReO_3 in Table 3.15, VO_2 prototype TiO_2 (rutile structure) in Table 3.16 and isostructural MoO_2 in Table 3.17.

Table 3.10: WO_3 P 4/n c c Z cell description.

formula	WO_3
space group	P 4/n c c Z (130)
a (Å)	5.290
c (Å)	7.913
V (Å^3 atom^{-1})	13.840
Z	4

atom	site	x	y	z
W	4 c	0.25	0.25	0.281
O	4 c	0.25	0.25	0.007
O	8 f	0.046	0.954	0.25

Table 3.11: WO_3 P 4/n m m Z cell description.

formula	WO_3
space group	P 4/n m m Z (129)
a (Å)	5.489
c (Å)	3.776
V (Å^3 atom^{-1})	14.220
Z	2

atom	site	x	y	z
W	2 c	0.25	0.25	0.988
O	2 c	0.25	0.25	0.496
O	4 d	0.0	0.0	0.0

Table 3.12: WO_3 P $\bar{4}$ 2_1 m cell description.

formula	WO_3
space group	P $\bar{4}$ 2_1 m (113)
a (Å)	7.498
c (Å)	4.014
V (Å^3 atom^{-1})	14.104
Z	4

atom	site	x	y	z
W	4 e	0.263	0.763	0.924
O	4 e	0.257	0.757	0.471
O	8 f	0.001	0.750	0.004

Table 3.13: WO_3 P c n b cell description.

formula	WO_3
space group	P c n b (60)
a (Å)	7.343
b (Å)	7.617
c (Å)	7.788
V (Å^3 atom^{-1})	13.614
Z	8

atom	site	x	y	z
W	8 d	0.252	0.026	0.280
O	8 d	0.999	0.043	0.212
O	8 d	0.294	0.260	0.260
O	8 d	0.291	0.012	0.007

Table 3.14: WO_3 P m n b cell description.

formula	WO_3
space group	P m n b (62)
a (Å)	7.389
b (Å)	7.746
c (Å)	7.925
V (Å^3 atom^{-1})	14.175
Z	8

atom	site	x	y	z
W	4 c	0.25	0.032	0.034
W	4 c	0.25	0.032	0.534
O	4 a	0.0	0.0	0.0
O	4 b	0.0	0.0	0.5
O	4 c	0.25	0.267	0.003
O	4 c	0.25	0.267	0.504
O	4 c	0.25	0.018	0.262
O	4 c	0.25	0.018	0.762

Table 3.15: WO_3 P 4/n c c Z cell description.

formula	ReO_3
space group	P m $\overline{3}$ m (221)
a (Å)	3.788
V (Å^3 atom^{-1})	13.593
Z	1

atom	site	x	y	z
Re	1 a	0.0	0.0	0.0
O	3 d	0.5	0.0	0.0

Table 3.16: TiO_2 (rutile) cell description.

formula	TiO_2
space group	P 4_2/m n m (136)
a (Å)	4.611
c (Å)	3.005
V (Å^3 atom^{-1})	10.648
Z	2

atom	site	x	y	z
Ti	2 a	0.0	0.0	0.0
O	4 f	0.304	0.304	0.0

Table 3.17: MoO_2 cell description.

formula	MoO_2
space group	P 4_2/m n m (136)
a (Å)	4.891
c (Å)	2.838
V (Å^3 atom^{-1})	11.318
Z	2

atom	site	x	y	z
Mo	2 a	0.0	0.0	0.0
O	4 f	0.285	0.285	0.0

3.2.2 Coulomb-potential-dependent decohesion of Magnéli phases

Cleavage was considered in those planes where each structure bears a resemblance to the V_2O_5 (002) layer structure and thus the largest difference in metal–oxygen bonding distances. This is the (002) plane for WO_3 phases P 4/ncc Z, P 4/nmm Z, P $\bar{4}2_1$m and P cnb and the (004) plane for the WO_3 phase P mnb. For MoO_2 and TiO_2 the same planes were used as for VO_2. Details on the methods used are discussed in Chapter 2.1.2. Due to large structural anisotropy for some phases, calculations to obtain the elastic properties were carried out with full structural relaxations at every volume, please see Chapter 2.1.2. No structural relaxation was allowed during the separation.

The decohesion energy and the elastic constant C_{44} are shown in Figure 3.7 as a function of the (original) distance d between the cleaved crystal layers. As the original distance between the cleaved crystal layers is increased from 1.1 to 2.8 Å, the decohesion energy decreases from 5.83 to 0.05 J m^{-2}. The data points were fitted with $a * 1/d * exp(-b * d)$ (screened Coulomb potential, with a and b as fitting parameters). Good agreement between the calculated decohesion energy and the fitting curve is observed. These data suggest that the bonding distance between the cleaved layers is one of the key factors determining the decohesion energy for the phases studied here. It is reasonable to assume that these easy cleaving planes in WO_3 and V_2O_5 are therefore responsible for the lubricating properties observed experimentally [49, 50]. This assumption is supported by the dependence of the elastic constant C_{44} on the distance between the cleaved layers (d), see Figure 3.7. As d is increased from 1.4 to 2.8 Å, C_{44} decreases from 139 to 25 GPa. It is evident that the decohesion energy and C_{44} can be estimated based on the layer distance only. This behaviour can be described by the screened Coulomb potential. Based on these results of the oxide phases calculated here, I propose that these correlations can be applied to other Magnéli phase oxides with a similar building principle of metal–oxygen octahedra.

As the decohesion energy and C_{44} are shown to depend primarily on the interlayer distance, it can be seen that this is not the case for the bulk modulus B. For the WO_3 phases, B is in the range from 78 to 159 GPa, thus in part close to B for V_2O_5 (87 GPa) but much lower than for the rutile structures (e.g. MoO_2 with 255 GPa). Since (at least) eleven different structures with composition WO_3 exist [56], these values may differ to a considerable degree due to

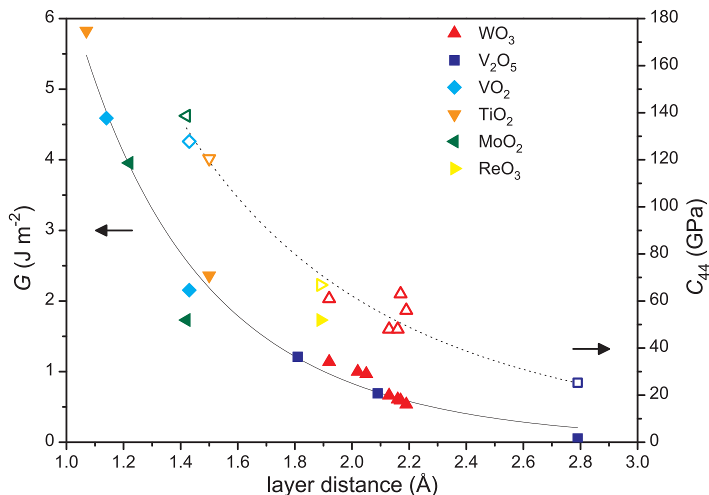

Figure 3.7: Decohesion energy G (filled symbols) and elastic constant C_{44} (open symbols) as a function of the original distance d between the cleaved layers. Data was fitted with $a * 1/d * exp(-b * d)$ (screened Coulomb potential, with a and b as fitting parameters).

very narrow stability regions within the phase diagram. The bulk modulus as well as the calculated lattice parameters, the number of formula units per unit cell Z, the elastic constant C_{44} and the decohesion energy in the plane with the longest interlayer bonding for VO_2, V_2O_5, MoO_2 and the five WO_3 phases are given in Table 3.18.

The different decohesion energies and C_{44} values of these oxides may be understood based on the electronic structure. Electron density distributions (EDDs) obtained by *ab initio* calculations were evaluated using VESTA [160]. EDDs are presented for ReO_3 in Figure 3.8 a, the WO_3 phase P 4/n c c Z in Figure 3.8 b and V_2O_5 in Figure 3.8 c. The WO_3 phase P 4/n c c Z was chosen since it bears the largest bonding length difference within the WO_6 polyhedron (1.79 to 2.17 Å). In general, these oxides are predominantly characterised by ionic bonding, due to the charge transfer from the metal to oxygen. To some extent, there is charge shared between these elements, giving rise to a smaller covalent contribution. In particular for the V_2O_5 vanadyl bond, covalent character is apparent, while it is not for the interlayer bonding. It is important to note that these EDDs never exhibit regions without charge (0 eV Å^{-3}), which may

Table 3.18: Calculated lattice parameters, number of formula units per unit cell (Z), bulk modulus B, elastic constant C_{44} and decohesion energy G for VO_2, V_2O_5, MoO_2 and five WO_3 phases.

structure	VO_2	V_2O_5	MoO_2	WO_3				
space group	$P\,4_2/mnm$	$P\,mmn$	$P\,4_2/mnm$	$P\,4/ncc$	$P\,4/nmm$	$P\,\bar{4}2_1m$	$P\,cnb$	$P\,mnb$
a (Å)	4.558	11.532	4.891	5.290	5.489	7.498	7.343	7.389
b (Å)		3.600					7.617	7.746
c (Å)	2.857	4.401	2.838	7.913	3.776	4.014	7.788	7.925
Z	2	2	2	4	2	4	8	8
B (GPa)	226.6	86.6	254.9	103.4	159.4	147.4	78.1	123.9
C_{44} (GPa)	127.8	25.3	138.7	62.7	61.2	55.6	48.3	47.9
cleavage plane	(002)	(002)	(002)	(002)	(002)	(002)	(002)	(004)
G ($J\,m^{-2}$)	2.15	0.05	1.73	0.59	1.14	0.54	0.66	0.61

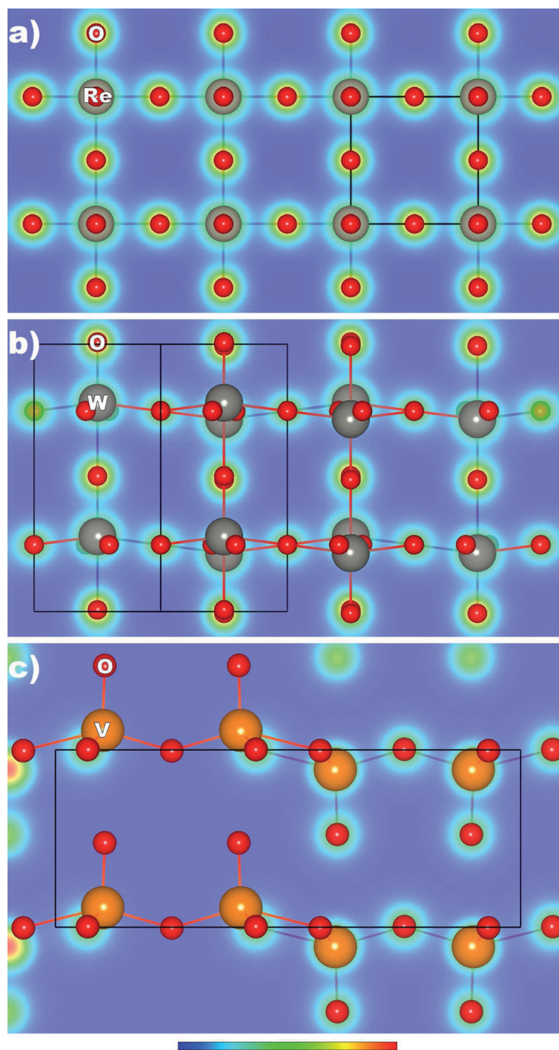

Figure 3.8: Structure and electron density distribution of **(a)** ReO_3 projected along the [100] axis, the EDD is shown for the (100) plane (increasing from 0.00 to 1.21 a.u.); **(b)** WO_3 (P 4/n c c Z) projected along the [$1\overline{1}0$] axis, the EDD is shown for the ($1\overline{1}0$) plane (increasing from 0.00 to 1.21 a.u.); **(c)** V_2O_5 projected along the [010] axis, the EDD is shown for the (040) plane (increasing from 0.00 to 2.13 a.u.). The black boxes mark the unit cells.

indicate that some minor metallic contributions are present. However, striking differences between these phases can be observed. In ReO_3 (Figure 3.8 a), P m$\overline{3}$m, the perfect octahedral coordination causes identical bonding for all six Re–O bonds. The bond length is 1.89 Å. In WO_3 (Figure 3.8 b), P 4/n c c Z, the WO_6 octahedron is distorted and the W cation is shifted from the centre. Thus, three different W–O bonds are formed: four identical bonds with a length of 1.92 Å parallel to the (1$\overline{1}$0) layer, a short 1.79 Å 'intralayer' bond and a long 2.17 Å 'interlayer' bond. Hence, in the shorter interaction there is more charge shared and a higher covalent contribution compared to the non-covalent longer interaction with less charge shared. This causes the formation of distinct layers within this crystal structure and thus a lower decohesion energy between these layers. In V_2O_5 (Figure 3.8 c), P m m n, the VO_6 octahedron is largely distorted. The actual coordination can be described as a square pyramid with an interlayer bond length of 2.79 Å. The short bond opposed is only 1.61 Å. This strong vanadyl bond is mainly of covalent character. The other bonds are characterised with bond lengths between 1.78 to 2.03 Å. Since the bonding differences are much larger than those in WO_3, clearly visible layers are formed, causing the extremely low decohesion energy between these layers.

3.2.3 Conclusions

It is evident that distorted metal–oxygen octahedra result in large layer distances and hence lower C_{44} values as compared to undistorted octahedra. Decohesion energy and C_{44} are inversely proportional to the distance between the cleaved crystal layers, and accordingly to the screened Coulomb potential, and thus the bond strength decreases rapidly as the distance is increased. This results in weak coupling between the layers which then causes the formation of easily plastically deformable structures, for instance WO_3 or V_2O_5. This behaviour can be understood based on changes in the crystal and electronic structure as displayed for ReO_3, WO_3 and V_2O_5. Thus, the relationship previously established for vanadium oxides applies to other Magnéli phases. The fact that structures such as WO_3 can also be described by the above-presented correlations provides the basis for quantum mechanical guided design of Magnéli phase structured solid lubricants, based on tailoring the layer distance by varying the chemical composition.

3.3 TiAlN–WN$_x$ thin film deposition

The following chapter contains results from a collaborative work with the Thin Film Physics Division group from Linköping University, Sweden, namely Davide G. Sangiovanni, Valeriu Chirita and Lars Hultman. They contributed ab initio data and took part in discussions which led to a publication [215]. The theoretical methods applied are in general similar to the methods described in Chapter 2.1.2 and are presented as Appendix A in more detail.

In this chapter, the combinatorial method has been employed to grow TiAlN–WN$_x$ films by Direct Current Magnetron Sputtering (DCMS) as well as by High Power Pulsed Magnetron Sputtering (HPPMS), leading to a gradient in chemical composition. TiAlN–WN$_x$ thin films have been deposited as described in Chapter 2.2.2. Analysis methods are discussed in Chapter 2.2.3 (SEM), 2.2.4 (EDX), 2.2.5 (XRD) and 2.2.6 (NI).

Based on these growth experiments as well as *ab inito* calculations, the following questions were answered:

1. How does the tungsten concentration influence the composition, structure and mechanical properties of cubic TiAlN–WN$_x$ deposited by combinatorial DCMS and HPPMS?

2. How does the degree of ionisation of film forming species influence the formation of TiAlN–WN$_x$ (while keeping the time averaged power constant)?

3.3.1 Thin film morphology and deposition rates

Cross-section FE-SEM images of the deposited TiAlN–WN$_x$ films are shown in Figures 3.9 a–f. Figures 3.9 a–c show the films deposited using DCMS with 14 at.% W concentration (thickness 2.0 µm), 32 at.% W (3.2 µm) and 51 at.% W (3.0 µm), respectively. These films exhibit a dense microstructure with fine, columnar-like grains. The thickness at the Ti-Al-rich side is significantly lower than at the W-rich side. As the magnitude of the deposition rate difference cannot be explained solely based on the difference in sputter yield, it is reasonable to assume that the here employed nitrogen partial pressure is sufficient to cause poisoning on the Ti-Al-target section, while the W-target section is

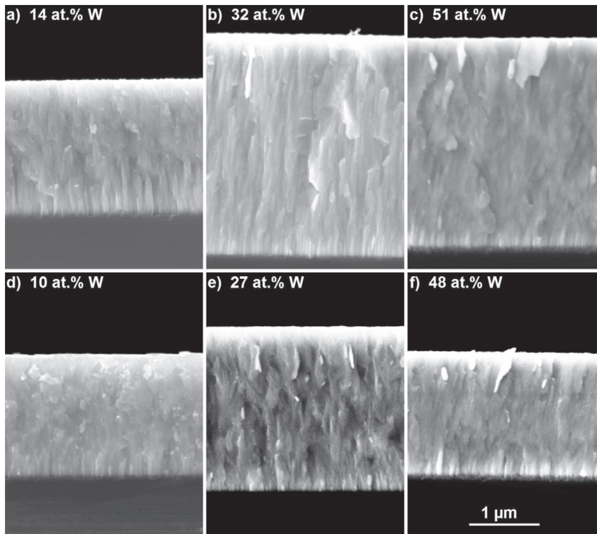

Figure 3.9: FE-SEM cross-section images of the TiAlN–WN_x films deposited with **(a–c)** DCMS (upper row) and **(d–f)** HPPMS (lower row). The tungsten concentration is increased from left to right images.

sputtered in metallic mode. This finding is supported by the visual impression of the colour of the plasma, which is different in front of the the Ti-Al-target section compared to the W-target section. Figures 3.9 d–f show the films deposited using HPPMS with 10 at.% W concentration (thickness 1.8 µm), 27 at.% W (2.3 µm) and 48 at.% W (1.8 µm), respectively. The films deposited with the high power pulsed plasma also show a dense microstructure with little defined columnar-like grains. The differences in film thickness are not as pronounced as in the DCMS case. During HPPMS, the Ti-Al-target section as well as the W-target section are sputtered in metallic mode. The relative deposition rate of HPPMS compared to DCMS is 90 % at the Ti-Al-rich side, 72 % in the middle and 60 % at the W-rich side.

The deposition rates using HPPMS are lower than those for DCMS, while the same time averaged power was applied (Table 2.1). Generally, this phenomenon is known and may be explained by the non-linear dependence of the sputter yield on the target potential [195] and other possible reasons, as already described in Chapter 2.2.1. As mentioned in Chapter 2.2.2, the cathode voltage

during HPPMS depositions reached −850 V and is thus much lower than the −435 V for DCMS.

Based on this relation, two-step simulations using TRansport-of-Ions-in-Matter (TRIM) simulations [216] have been carried out to estimate the deposition/sputter rates adopting the same methodology as employed by Emmerlich *et al.* [195]. It should be noted, though, that this is only a rough estimation because of the high nitrogen partial pressure and the manifold of possible interactions that are not considered here. Maximum sputter rates using the measured voltage and current data during depositions are calculated for sputtering the single metal species in pure self-sputtering mode and in pure argon, giving the lower and the upper limits of the deposition rate, respectively. Thus, the HPPMS rate for Ti is estimated to be within a range of 0 to 86 % of the DCMS rate, for Al within 17 to 90 % and for W within 1 to 88 %. Hence, a lower deposition rate is expected for HPPMS compared to DCMS for all compositions, consistent with the experimental findings. For the Ti-Al-rich side, the measured HPPMS/DCMS deposition rate ratio of 90 % is at the upper calculated limit, which would indicate that the sputter rate during HPPMS is mainly determined by argon sputtering and hence the metal ion fraction should be very low – as in the DCMS mode. However, different target conditions would have to be taken into account. Considering that Ti-Al-rich target side is sputtered in poisoned mode for DCMS and in metallic mode for HPPMS, this comparison is not straightforward since the DCMS-deposited film would be expected to be thicker if sputtered in metallic mode and thus the HPPMS/DCMS ratio would be smaller. This ratio would then be significantly smaller than the calculated maximum of 86/90 % for Ti/Al and accordingly the metal ion fraction is supposed to be larger than for DCMS. The W-rich side is sputtered in metallic mode for both DCMS and HPPMS, allowing reasonable comparison of the HPPMS/DCMS deposition rates for tungsten. For the W-rich side, the measured rate of 60 % is within the calculated sputter rate range of 1 to 88 % and about a third of the sputtered W can be expected to be caused by self-sputtering. Hence, a notable W ion fraction populates the plasma and contributes to the film formation.

3.3.2 Thin film composition

Figure 3.10 shows the film composition for the depositions with DCMS and HPPMS. Uniform W gradients of 10 to 52 at.% for DCMS and 7 to 54 at.% for HPPMS are obtained, while the combined concentrations of Ti and Al are de-

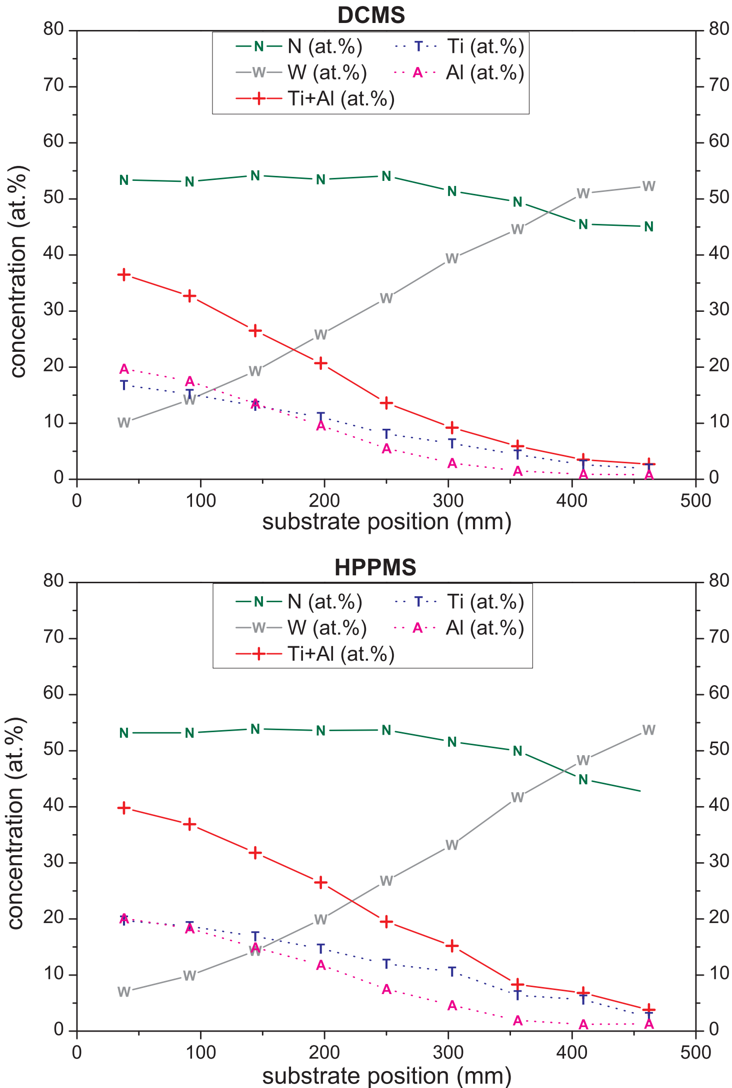

Figure 3.10: Composition of the films deposited with DCMS (top) and HPPMS (bottom), measured by EDX.

creased from 37 to 2 at.% and 40 to 4 at.%, respectively. The Al concentration decreases slightly faster than the Ti concentration, indicating preferential re-sputtering of Al at higher W concentrations. For example, as the W concentration is increased from 10 to 32 /33 at.% for DCMS/HPPMS, the Al concentration decreases by 14 at.% while the Ti concentration only decreases by 9 /8 at.%, respectively. A nitrogen concentration of about 53 to 54 at.% is detected for DCMS- and HPPMS-deposited films at W concentrations ranging from 10 to 32 at.% and from 7 to 27 at.%, respectively. Over-stoichiometric N is often reported for titanium nitride-based thin films, which can be due to vacancies in the metal sub-lattice [10, 11] or due to interstitial N incorporation during non-equilibrium film growth [6, 8, 13, 14]. As the W concentration is further increased, the N concentration decreases, reaching 45 and 42 at.% N at 52 and 54 at.% W for DCMS and HPPMS, respectively. Thus, the N concentration approaches the stoichiometry of the W_2N phase which is expected in thermodynamic equilibrium. A decreasing N concentration was also reported as the W concentration of Mo-W-N films was increased [217]. The authors attributed this to be due to the lower chemical affinity of N to W as compared to Mo [217]. It is also reported that the N concentration in cubic tungsten nitride can be much higher than the stoichiometric value of 33 at.% for the thermodynamically stable bulk W_2N phase. Nitrogen concentrations of 55 at.% [66], 58 at.% [65] and 63 at.% [67] were observed. The N concentration in WN_x films was reported to depend to a large extent on the deposition conditions, in particular nitrogen pressure, deposition rate and substrate temperature. The higher the ion/adatom mobility due to ion bombardment and heating, the lower the N concentration approaching the stoichiometry of the stable W_2N equilibrium phase [65–67]. Another mechanism contributing towards a reduced N concentration at increased W concentrations may be preferential etching of N by the heavier W.

3.3.3 Thin film structure and lattice parameter

Figure 3.11 shows the X-ray diffraction patterns of the TiAlN–WN_x films deposited with DCMS (upper part) and HPPMS (lower part). From each deposition, diffractograms are shown for the four compositions investigated for nanoindentation. Neither hexagonal or tetragonal tungsten nitride phases nor the hexagonal aluminium nitride phase are present in these films. The films deposited with DCMS show only the cubic B1 (NaCl) phase, except for the film

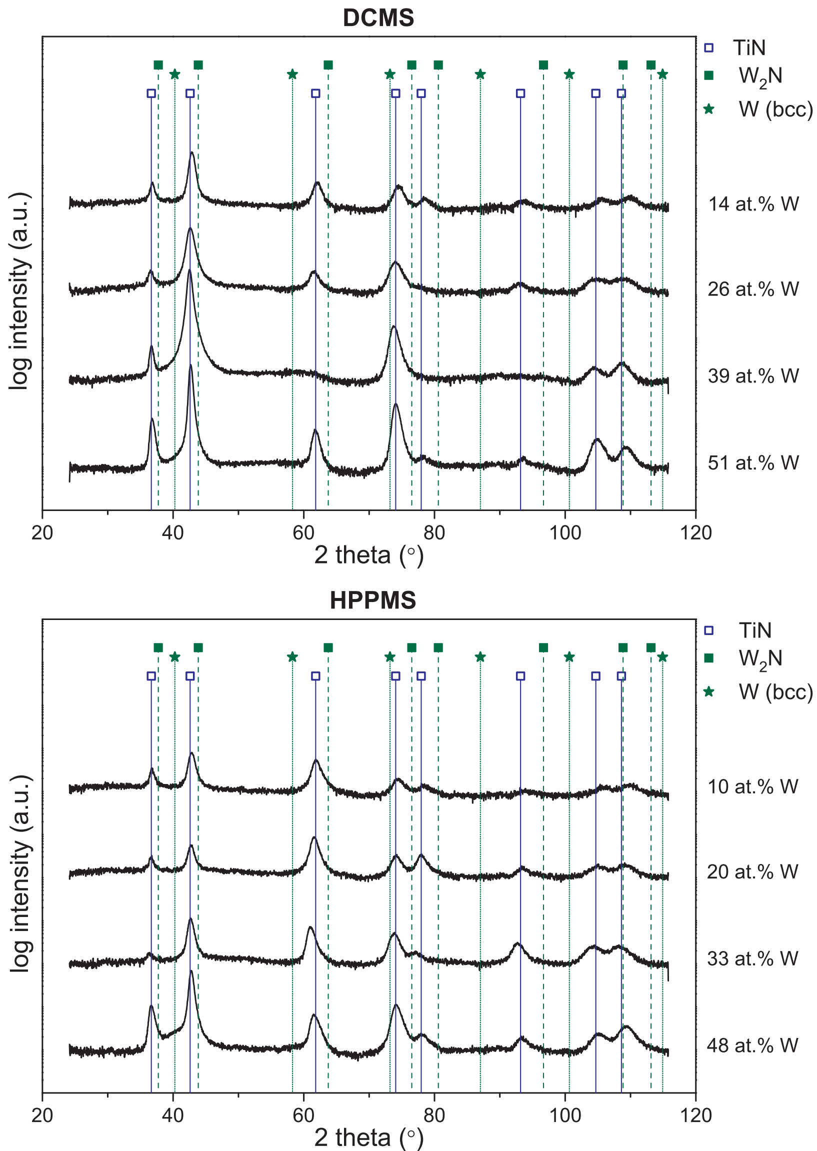

Figure 3.11: Diffraction patterns of the TiAlN–WN$_x$ films deposited with DCMS (upper part) and HPPMS (lower part) at different tungsten concentrations. Reference TiN [JCPDS card No. 38-1420], W_2N [JCPDS card No. 25-1257] and W [JCPDS card No. 4-806] are shown by vertical lines.

with a W concentration of 52 at.% where a very small peak indicates the presence of bcc tungsten. XRD data of the films deposited with HPPMS containing 54 at.% W indicate the formation of bcc tungsten. The film with 48 at.% W exhibits a shoulder on the (200) peak suggesting the presence of minute quantities of bcc W. This may be a consequence of the large W deposition rate, a too low nitrogen (partial) pressure, etching of N by W and the comparatively small heat of formation. The N concentration in tungsten nitride films is reported to decrease as the cathode power/deposition rate is increased and as the nitrogen pressure is decreased [65]. The heat of formation for W_2N is $\Delta H \approx 71$ kJ mol^{-1} and thus much lower than $\Delta H \approx 335$ kJ mol^{-1} for TiN [57]. The presence of metallic tungsten is often reported for tungsten nitride films [65, 66, 68, 218] or for tungsten-rich Mo-W-N films for W concentrations >34 at.% [217].

Besides the presence of the metallic bcc tungsten phase at very high W concentrations, all films show diffraction lines of the B1 TiN structure. Figure 3.12 shows the lattice parameter of the TiAlN–WN_x films obtained from the XRD patterns and by *ab initio* calculations. The lattice parameter for the as-deposited films is averaged from (111) and (200) peaks. The error bars display the (111) and (200) values and thus give information about the picostructural deviation from the perfect cubic lattice. These deviations are probably caused by ion bombardment and ion implantation, giving rise to defects in the crystal structure which cause micro-strain [219, 220]. Deviations are larger for the HPPMS-deposited films, which may be due to the larger degree of ionisation of the plasma and the higher deposited flux during the pulse. As the W concentration is increased, the lattice parameter of the films deposited with DCMS increase from 4.204 Å for 10 at.% W to 4.247 Å for 26 at.% W. As the W concentration is further increased to levels above 29 at.% W, the lattice parameter decreases to 4.224 Å for 52 at.% W. The lattice parameter of the films deposited with HPPMS is increased from 4.222 Å for 7 at.% W to 4.252 Å for 27 at.% W, while at higher W concentrations a decrease to 4.218 Å for 54 at.% W is measured. Thus, the substitution of Ti and Al by W leads to an increasing average lattice parameter for DCMS to a W concentration of $\approx$29 at.% and for HPPMS to a W concentration of $\approx$27 at.%. Above these concentrations the average lattice parameter does no longer increase as predicted by the *ab initio* calculations. At the same time, less nitrogen is incorporated into the films. The lattice parameter obtained by the *ab initio* calculations for $(Ti_xAl_xW_{1-2x})N$ phases show an increase from 4.175 to 4.357 Å as the W concentration is increased from 0 to 50 at.%. It should be noted that for the phase with 50 at.% W (WN)

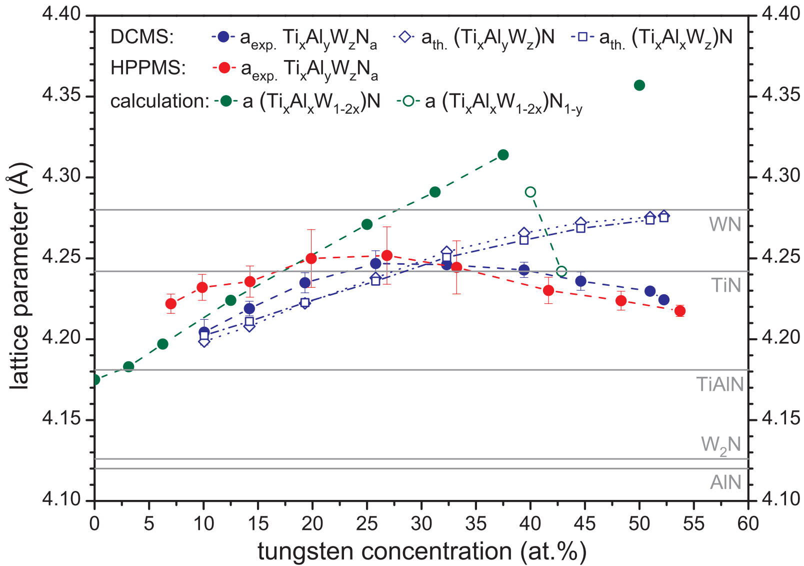

Figure 3.12: Lattice parameter of the TiAlN–WN_x films deposited with DCMS (blue) and HPPMS (red) are shown as filled circles. Data obtained by *ab initio* calculations are shown as filled green circles for $(Ti_xAl_xW_{1-2x})N$ and as open green circles when including nitrogen vacancies ($Ti_{0.125}Al_{0.125}W_{0.75}N_{0.875}$ and $Ti_{0.125}Al_{0.125}W_{0.75}N_{0.75}$). Theoretical lattice parameters for (W,Ti,Al)N derived from literature values of the binary phases (TiN [JCPDS card No. 38-1420], AlN [JCPDS card No. 46-1200] and WN [65]) using the metal concentrations of the DCMS-deposited films are shown in open blue symbols, displaying data for the actual metal ratios $(Ti_xAl_yW_z)N$ (diamonds) and assuming a constant Ti:Al ratio of 1:1 $(Ti_xAl_xW_z)N$ (squares).

the elastic constant C_{44} is negative, suggesting structural instability. This is consistent with previous calculations [221].

Composition-induced changes in lattice parameter closely following Vegard's law were reported for Ti-Al-N [24, 36–38]. For example, the lattice parameter decreased from 4.247 to 4.209 Å as the Al concentration was increased from 0 to 41 at.% [37]. *Ab initio* calculations for $Ti_{1-x}Al_xN$ also showed a linear dependence of the lattice parameter on the AlN fraction x up to $x = 0.7$ based on the rules of mixture [38]. Likewise, the lattice parameter of sputtered cubic $Cr_{1-x}Al_xN$ films continuously decreased from 4.171 to 4.113 Å as the Al concentration was increased from 5 to 35 at.% with *ab initio* calculations showing similar results [222].

Assuming that Vegard's law can be applied to the system investigated here, theoretical lattice parameters for $(Ti_xAl_yW_z)N$ were derived using literature values of the binary phases TiN [JCPDS card No. 38-1420], AlN [JCPDS card No. 46-1200] and WN_x ($x \approx 1$) [65] and the metal concentrations of the DCMS-deposited films assuming an N concentration of 50 at.%. Thus, differences compared to the experimentally obtained lattice parameters may be attributed to differences in the N concentration and other growth induced defects. The results are shown in Figure 3.12 as blue open symbols; for the actual metal concentrations with a Ti:Al:W ratio of x:y:z $(Ti_xAl_yW_z)N$ (diamonds) and assuming a constant Ti:Al ratio of 1:1 (based on the sum of both concentrations) with a Ti:Al:W ratio of x:x:z $(Ti_xAl_xW_z)N$ (squares). As the W concentration is increased, the lattice parameter increases for both compositions. The differences in the lattice parameter due to the change in the Ti:Al ratio, which can be assessed from Figure 3.10, are rather small. The largest deviations from this ratio occur at high W concentrations, where the fractions of Ti and Al and thus their influence on the lattice parameter are negligible. I suggest that the deviation between these calculated and the experimentally obtained lattice parameter can be attributed to defects in the crystal lattice. It is reasonable to assume that a reduction in N concentration is primarily responsible for this difference. This hypothesis is supported by the *ab initio* calculations for N-deficient phases $Ti_{0.125}Al_{0.125}W_{0.75}N_{0.875}$ and $Ti_{0.125}Al_{0.125}W_{0.75}N_{0.75}$, shown as open green circles in Figure 3.12. While maintaining a constant Ti:Al:W ratio of 1:1:6 (equal to 38 at.% W without N vacancies), the lattice parameter decreases from 4.314 to 4.242 Å for the phase with an N concentration of 43 at.% (resulting in 43 at.% W). This is not only consistent with the reported

composition and lattice parameter data trend, but does also agree rather well with the magnitude of the experimental lattice parameter.

A similar tendency was reported for $Ti_{1-x}W_xN$ films with $0 \leq x \leq 0.7$ [223]. As the W concentration was increased, the lattice parameter initially increased and then decreased. This was attributed to be due to a simultaneous N concentration decrease [223], which is in agreement with the findings presented here. Though, as mentioned before, tungsten nitride phases (W_2N or WN_x) can contain up to 63 at.% N [65–67] and thus much more than the W_2N stoichiometry proposes. It has been suggested that in the W_2N structure, additional nitrogen occupies vacant octahedral sites, enlarging the lattice parameter [68, 69]. The lattice parameter for WN_x with $x \approx 1$ was measured to be about 4.28 Å [65, 69], while the value for a stoichiometric W_2N bulk sample is 4.126 Å [JCPDS card No. 25-1257]. In addition, compressive stress in the thin films might also serve for a larger lattice parameter. For WN_x films, a larger lattice parameter compared to theoretical values is reported for N concentrations of 55 at.%, which decreases as the N concentration is decreased [224]. Similar correlations between the N concentration and the lattice parameter were reported for TiN, although the linearity of this relation and values for over-stoichiometric N concentrations are somewhat ambiguous, please see Chapter 1.2.1. Nitrogen vacancies may cause the lattice parameter shrinkage and *ab initio* calculations support this assumption [9]. For N concentrations above 50 at.%, due to N incorporation at interstitial positions, lattice parameters that exceed the common value for bulk samples are reported [6, 8, 13, 14]. Based on these data, it can be concluded that the correlation between lattice parameter and W concentration can only be understood if changes in the N concentration are considered. If TiAlN is alloyed with W, the expected lattice parameter increase is counteracted by a reduced N concentration.

3.3.4 Young's modulus and hardness of the thin films

Young's modulus and hardness for the films are shown in Figure 3.13 as well as Young's modulus from the *ab initio* data. For the films deposited with DCMS, Young's modulus is around 385 to 400 GPa and hardness is around 29 to 31 GPa. Thus, there is no significant variation observed as the W concentration is increased. For the films deposited with HPPMS, Young's modulus is in the range of 430 to 480 GPa and hardness is in the range of 34 to 38 GPa. As the W concentration is increased, the average Young's modulus and hardness

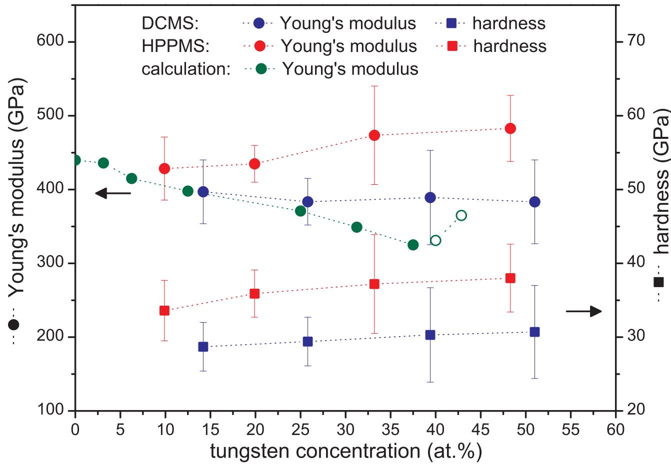

Figure 3.13: Young's modulus (circles) and hardness (squares) determined by nanoindentation for the films deposited with DCMS (blue) and HPPMS (red). The Young's modulus obtained by *ab initio* calculations is shown as filled green circles for $(Ti_xAl_xW_{1-2x})N$ and as open green circles when including nitrogen vacancies ($Ti_{0.125}Al_{0.125}W_{0.75}N_{0.875}$ and $Ti_{0.125}Al_{0.125}W_{0.75}N_{0.75}$).

values increase. Considering the error bars, this increase is not significant. *Ab initio* calculations show a continuous decrease in Young's modulus from 440 to 325 GPa as the W concentration is increased from 0 to 37.5 at.%, see Table 3.19. The calculated data show reasonable agreement with the experimental Young's modulus values (especially DCMS) for W concentrations $<$30 at.%. For W concentrations where N deficient compositions were measured, the calculated Young's modulus values are significantly smaller than the experimentally determined values. However, as the N deficiency is included in the calculations, the calculated elasticity approaches the values measured, see the open green circles in Figure 3.13. Upon insertion of N vacancies, the Young's modulus increases to 365 GPa for $Ti_{0.125}Al_{0.125}W_{0.75}N_{0.75}$. The differences to the values for DCMS and HPPMS are about 6 and 30 %, respectively. To a smaller extent, these differences may be attributed to an expected increase in Poisson's ratio with increasing W concentration [225, 226], which could not be considered for the experimental values. The calculated data for different compositions – lattice parameter, bulk, Young's and shear modulus – are listed in Table 3.19. I suggest that the N vacancies in the W-rich deposited films might

Table 3.19: Lattice parameter, bulk, Young's and shear modulus obtained by *ab initio* calculations for different nitride compositions.

composition	a (Å)	B (GPa)	E (GPa)	G (GPa)
$Ti_{0.5}Al_{0.5}N$	4.175	269	440	179
$Ti_{0.47}$ $Al_{0.47}$ $W_{0.06}N$	4.183	274	436	177
$Ti_{0.44}$ $Al_{0.44}$ $W_{0.12}N$	4.197	277	415	166
$Ti_{0.375}Al_{0.375}W_{0.25}N$	4.224	282	398	157
$Ti_{0.25}$ $Al_{0.25}$ $W_{0.50}N$	4.271	306	371	143
$Ti_{0.19}$ $Al_{0.19}$ $W_{0.62}N$	4.291	315	349	133
$Ti_{0.125}Al_{0.125}W_{0.75}N$	4.314	326	325	122
$Ti_{0.125}Al_{0.125}W_{0.75}N_{0.875}$	4.291	311	331	125
$Ti_{0.125}Al_{0.125}W_{0.75}N_{0.75}$	4.242	318	365	140

be the reason for the relatively uniform mechanical properties, counteracting the decrease in Young's modulus due to the substitution of Ti and Al by W in analogy to the previously discussed lattice parameter data.

Different results concerning N vacancies have been found for TiN_x films [15]. When decreasing x from 1 to 0.67, increasing the N vacancy concentration, Young's modulus was decreased. The different N concentration in the stable phases TiN and W_2N and hence the phase stability might explain the contrary behaviour compared to this work. Young's modulus and hardness of WN films with a stoichiometry close to unity were reported to be 380 GPa and 30 GPa, respectively [224]. Hardness for tungsten nitride thin films was found to be within 20 to 40 GPa, with this broad range being influenced by differing N concentrations and microstructures depending on the deposition conditions [224, 227]. Young's modulus and hardness of Mo-W-N films were shown to increase with increasing W concentration [217]. As the W concentration was increased from 0 to 37 at.%, Young's modulus and hardness were reported to increase from about 300 to 586 GPa and 25 to 47 GPa, respectively, while simultaneously the N concentration decreased. The strengthening was attributed to solid solution hardening, grain refinement and stress within the films. At W concentrations above 37 at.%, Young's modulus and hardness rapidly decreased due to a phase separation.

The HPPMS-deposited films have 30 to 95 GPa higher Young's modulus and 5 to 7 GPa higher hardness than the DCMS films. This may be explained by the higher (metal) ion density in the plasma, causing film densification. The intensified ion bombardment is known to increase micro-strain [219, 220] (see

Figure 3.12) and hardness. In addition, high ion density during deposition usually leads to very dense and smooth films [186, 187] with a finer grained microstructure. The smaller grain size may lead to higher hardness due to the Hall-Petch relationship, which was observed for WN_x films [228]. Increased hardness of HPPMS- compared to DCMS-deposited films has also been observed for CrN/NbN, which was explained by the higher intrinsic stresses in the HPPMS-deposited film [229]. For AlN, a hardness increase of 10 GPa by HPPMS deposition compared to DCMS was reported and assumed to be due to the enhanced ion bombardment [230]. Increased Young's modulus and hardness of CrN deposited by modulated pulsed power magnetron sputtering [231] was attributed to the higher film density, decreased grain size and a smooth surface due to the intensified ion bombardment [231].

3.3.5 Conclusions

TiAlN–WN_x films were grown by combinatorial DCMS and HPPMS. The influence of the tungsten concentration on structure and mechanical properties of cubic TiAlN–WN_x was investigated experimentally and by *ab initio* methods. The films were grown with a uniform W gradient of 10 to 52 at.% by DCMS and 7 to 54 at.% by HPPMS. An N concentration of about 53 to 54 at.% was detected for DCMS- and HPPMS-deposited films up to W concentrations of 32 and 27 at.%, which decreased to 45 and 42 at.% N at 52 and 54 at.% W for DCMS and HPPMS, respectively. The substitution of Ti and Al by W within the cubic B1 structure leads to an increased average lattice parameter for W concentrations up to ≈29 at.% for DCMS and ≈27 at.% for HPPMS, while at higher W concentrations the lattice parameter decreased. The reduction in N concentration is primarily responsible for this lattice parameter decrease. The lattice parameter obtained by *ab initio* calculations increased as the W concentration was increased from 0 to 50 at.%. Nitrogen vacancies formed at high W concentrations cause the lattice parameter to decrease, which is in good agreement with the experimental results. Young's modulus and hardness are around 385 to 400 GPa and 29 to 31 GPa for DCMS and 430 to 480 GPa and 34 to 38 GPa for HPPMS, respectively, showing no significant trend as the W concentration is changed. HPPMS-deposited films exceed DCMS films in Young's modulus and hardness, which may be a consequence of the larger degree of ionisation in the HPPMS plasma. It is reasonable to assume that especially the ionised film forming species may contribute towards film densification and

N vacancy formation. Calculated data show a continuous decrease in Young's modulus as the W concentration is increased. Upon insertion of N vacancies at high W concentrations, the calculated Young's modulus increases. Hence, the experimental elasticity data can be understood by considering the combined effects of the rules of mixture and the N vacancy formation.

4 Conclusions

4.1 Magnéli phase oxides conclusions

The objective of this work was to contribute towards understanding of the correlation between composition, structure, elastic and mechanical properties of Magnéli phase oxides. The strategy was to apply *ab initio* calculations to obtain structural data, bulk modulus, elastic constant C_{44} and decohesion energies and correlate these with the electronic structure.

Seven different vanadium oxides VO_x ($1 \leq x \leq 2.5$) have been investigated, namely VO, V_2O_3, VO_2, V_6O_{13}, V_4O_9, V_3O_7 and V_2O_5. As the V valency is increased from 3 to 5, crystal structure and chemical bonding changes are observed. The C_{44} values for V_6O_{13}, V_4O_9, V_3O_7 and V_2O_5 are significantly lower than those for V_2O_3 and VO_2. C_{44} decreases by 83 %, whereas the bulk modulus values decrease by 61 %, leading to an increase in the B/C_{44} ratio from 1.4 to 3.4. This is consistent with calculated decohesion energies for cleavage in VO_2 and V_2O_5. When cleaving V_2O_5 in the (002) plane, decohesion energy is extremely low with 0.05 $J\,m^{-2}$, as compared to VO_2. Furthermore, the calculated decohesion energies are inversely proportional to the original distance between the cleaved layers. Thus, it can be expected that this easy cleaving plane enables plastic deformation and is therefore responsible for the vanadium pentoxide's lubricating properties that have been reported in literature. This behaviour can be understood based on V valency induced changes in the electronic structure as well as in the chemical bonding. In the phases exhibiting high C_{44} values, V_2O_3 and especially in VO_2, there are only very small regions with low electron density between the ions, or rather between the V–O polyhedra, implying relatively strong bonding. In the phases exhibiting low C_{44} values, V_6O_{13}, V_4O_9, V_3O_7 and especially V_2O_5, there are very large regions with low electron density between the V–O polyhedra, or rather between the layers. Due to the screened Coulomb potential between these layers, the bond strength decreases rapidly as the distance is increased, resulting in weak coupling between the layers which then causes the formation of easily plastically deformable structures.

To deepen understanding of the correlation between the (electronic) structure and the elasticity as well as the decohesion energies of Magnéli phase oxides, studies have been extended to five WO_3 phases, a WO_3 parent structure ReO_3, MoO_2 and TiO_2 (rutile), which were compared to VO_2 and V_2O_5. As the original distance between the cleaved crystal layers is increased from 1.1 to 2.8 Å, the decohesion energy decreases from 5.83 to 0.05 J m^{-2}, while C_{44} values show a similar dependence. Good agreement between the calculated decohesion energy–layer distance relation and the fitting curve $a * 1/d * exp(-b * d)$ with respect to the screened Coulomb potential is observed. While ReO_3 features a perfect octahedral coordination causing identical bonding for all six metal–oxygen bonds, these octahedra are distorted in structures such as WO_3 and V_2O_5, causing the formation of distinct layers within these crystal structures. It is evident that the distorted metal–oxygen octahedra result in large layer distances and hence lower C_{44} values as compared to undistorted octahedra. Decohesion energy and C_{44} are inversely proportional to the distance between the cleaved crystal layers, and accordingly to the screened Coulomb potential, and thus the bond strength decreases rapidly as the distance is increased. This results in weak coupling between the layers which then causes the formation of easily plastically deformable structures, for instance WO_3 or V_2O_5. This behaviour can be understood based on changes in the crystal and electronic structure as displayed for ReO_3, WO_3 and V_2O_5. Based on these results of the oxide phases calculated here, I propose that these correlations can be applied to other Magnéli phase oxides with a similar building principle of metal–oxygen octahedra. The fact that structures such as WO_3 can also be described by the above-presented correlations provides the basis for quantum mechanical guided design of Magnéli phase structured solid lubricants, based on tailoring the layer distance by varying the chemical composition.

4.2 TiAlN–WN$_x$ conclusions

The objective was to contribute towards understanding the correlation between composition, structure and mechanical properties of cubic TiAlN alloyed with tungsten. Therefore, a combinatorial method was employed to grow TiAlN–WN$_x$ films, leading to a gradient in the W concentration. Two different sputtering techniques (DCMS and HPPMS) were used to investigate the influence of the

degree of ionisation of film forming species on the formation of TiAlN–WN_x films. During all depositions the time averaged power was kept constant.

The rectangular sputter target was build up of two triangular-shaped segments; one sintered Ti-Al (50:50), the other W, arranged in a way that a W composition gradient on the deposited films ranging from 10 to 52 at.% for DCMS and from 7 to 54 at.% for HPPMS was obtained. An N concentration of about 53 to 54 at.% was detected for DCMS- and HPPMS-deposited films up to W concentrations of 32 and 27 at.%, which decreased to 45 and 42 at.% N at 52 and 54 at.% W for DCMS and HPPMS, respectively. The substitution of Ti and Al by W within the cubic B1 structure led to an increased average lattice parameter for W concentrations up to ≈29 at.% for DCMS and ≈27 at.% for HPPMS, while at higher W concentrations the lattice parameter decreased. The reduction in N concentration is primarily responsible for this lattice parameter decrease. The lattice parameter obtained by *ab initio* calculations increased as the W concentration was increased from 0 to 50 at.%. Nitrogen vacancies formed at high W concentrations cause the lattice parameter to decrease, which is in good agreement with the experimental results. Young's modulus and hardness were around 385 to 400 GPa and 29 to 31 GPa for DCMS and 430 to 480 GPa and 34 to 38 GPa for HPPMS, respectively, showing no significant trend as the W concentration was changed. HPPMS-deposited films exceeded DCMS films in Young's modulus and hardness, which may be a consequence of the larger degree of ionisation in the HPPMS plasma. It is reasonable to assume that especially the ionised film forming species may contribute towards film densification and N vacancy formation. Calculated data showed a continuous decrease in Young's modulus as the W concentration was increased. Upon insertion of N vacancies at high W concentrations, the calculated Young's modulus increased. Hence, the experimental elasticity data can be understood by considering the combined effects of the rules of mixture and the N vacancy formation.

5 Bibliography

[1] Referat Öffentlichkeitsarbeit, ed. *Rahmenprogramm: Werkstoffinnovationen für Industrie und Gesellschaft – WING*. Bundesministerium für Bildung und Forschung (BMBF) (2003).

[2] P. Ehrlich. *Z. Anorg. Chem.* 259(1-4), 1 (1949).

[3] B. Holmberg. *Acta Chem. Scand.* 16, 1255 (1962).

[4] N. Schönberg. *Acta Chem. Scand.* 8, 213 (1954).

[5] A. N. Christensen. *Acta Chem. Scand. A* 32, 89 (1978).

[6] J.-E. Sundgren. *Thin Solid Films* 128(1-2), 21 (1985).

[7] S. Nagakura, T. Kusunoki, F. Kakimoto and Y. Hirotsu. *J. Appl. Crystallogr.* 8(1), 65 (1975).

[8] J. H. Kang and K. J. Kim. *J. Appl. Phys.* 86(1), 346 (1999).

[9] N. J. Ashley, R. W. Grimes and K. J. McClellan. *J. Mater. Sci.* 42, 1884 (2007).

[10] J.-E. Sundgren, B.-O. Johansson, S.-E. Karlsson and H. T. G. Hentzell. *Thin Solid Films* 105(4), 367 (1983).

[11] H. Bender, J. Portillo and W. Vandervorst. *Surf. Interface Anal.* 14(6-7), 337 (1989).

[12] A. Brager. *Acta Physicochim. URSS* 11, 617 (1939).

[13] A. J. Perry, M. Georgson and W. D. Sproul. *Thin Solid Films* 157(2), 255 (1988).

[14] J.-P. Noël, D. C. Houghton, G. Este, F. R. Shepherd and H. Plattner. *J. Vac. Sci. Technol. A* 2(2), 284 (1984).

[15] C.-S. Shin, D. Gall, N. Hellgren, J. Patscheider, I. Petrov and J. E. Greene. *J. Appl. Phys.* 93(10), 6025 (2003).

[16] G. Lemperière. *Thin Solid Films* 111, 339 (1984).

[17] K.-H. Habig, W. Evers and H. E. Hintermann. *Materialwiss. Werkstofftech.* 11(5), 182 (1980).

[18] W.-D. Münz. *Thin Solid Films* 96, 79 (1982).

[19] W. D. Sproul and R. Rothstein. *Thin Solid Films* 126(3-4), 257 (1985).

[20] M. Wittmer. *Appl. Phys. Lett.* 36(6), 456 (1980).

[21] S.-Q. Wang, I. Raaijmakers, B. J. Burrow, S. Suthar, S. Redkar and K.-B. Kim. *J. Appl. Phys.* 68(10), 5176 (1990).

[22] J. Desmaison, P. Lefort and M. Billy. *Oxid. Met.* 13(3), 203 (1979).

[23] W.-D. Münz. *J. Vac. Sci. Technol. A* 4(6), 2717 (1986).

[24] O. Knotek, M. Böhmer and T. Leyendecker. *J. Vac. Sci. Technol. A* 4(6), 2695 (1986).

[25] O. Knotek, W.-D. Münz and T. Leyendecker. *J. Vac. Sci. Technol. A* 5(4), 2173 (1987).

[26] D. McIntyre, J. E. Greene, G. Hakansson, J.-E. Sundgren and W.-D. Münz. *J. Appl. Phys.* 67(3), 1542 (1990).

[27] R. Cremer, K. Reichert and D. Neuschütz. *Surf. Coat. Technol.* 142-144, 642 (2001).

[28] S. PalDey and S. C. Deevi. *Mater. Sci. Eng. A* 342(1-2), 58 (2003).

[29] H. Holleck. *Surf. Coat. Technol.* 36(1-2), 151 (1988).

[30] P. Spencer. *Z. Metallkd.* 92(10), 1145 (2001).

[31] P. H. Mayrhofer, D. Music and J. M. Schneider. *Appl. Phys. Lett.* 88(7), 071922 (2006).

[32] J. C. Schuster and J. Bauer. *J. Solid State Chem.* 53(2), 260 (1984).

[33] R. Prange, R. Cremer and D. Neuschütz. *Surf. Coat. Technol.* 133-134, 208 (2000).

[34] R. Cremer, M. Witthaut, A. von Richthofen and D. Neuschütz. *Fresenius J. Anal. Chem.* 361(6), 642 (1998).

[35] P. H. Mayrhofer, D. Music and J. M. Schneider. *J. Appl. Phys.* 100(9), 094906 (2006).

[36] K. Kutschej, P. H. Mayrhofer, M. Kathrein, P. Polcik, R. Tessadri and C. Mitterer. *Surf. Coat. Technol.* 200(7), 2358 (2005).

[37] Z.-J. Liu, P. W. Shum and Y. G. Shen. *Thin Solid Films* 468(1-2), 161 (2004).

[38] B. Alling, A. V. Ruban, A. Karimi, O. E. Peil, S. I. Simak, L. Hultman and I. A. Abrikosov. *Phys. Rev. B* 75(4), 045123 (2007).

[39] A. Kimura, H. Hasegawa, K. Yamada and T. Suzuki. *Surf. Coat. Technol.* 120-121, 438 (1999).

[40] R. J. Rodríguez, J. A. García, A. Medrano, M. Rico, R. Sánchez, R. Marénez, C. Labrugère, M. Lahaye and A. Guette. *Vacuum* 67(3-4), 559 (2002).

[41] E. Pflüger, A. Schröer, P. Voumard, L. Donohue and W.-D. Münz. *Surf. Coat. Technol.* 115(1), 17 (1999).

[42] Q. Luo, W. M. Rainforth and W.-D. Münz. *Wear* 225-229(1), 74 (1999).

[43] P. E. Hovsepian, D. B. Lewis, Q. Luo, W.-D. Münz, P. H. Mayrhofer, C. Mitterer, Z. Zhou and W. M. Rainforth. *Thin Solid Films* 485(1-2), 160 (2005).

[44] C. P. Constable, J. Yarwood, P. E. Hovsepian, L. A. Donohue, D. B. Lewis and W.-D. Münz. *J. Vac. Sci. Technol. A* 18(4), 1681 (2000).

[45] D. B. Lewis, S. Creasey, Z. Zhou, J. J. Forsyth, A. P. Ehiasarian, P. E. Hovsepian, Q. Luo, W. M. Rainforth and W.-D. Münz. *Surf. Coat. Technol.* 177-178, 252 (2004).

[46] P. H. Mayrhofer, P. E. Hovsepian, C. Mitterer and W.-D. Münz. *Surf. Coat. Technol.* 177-178, 341 (2004).

[47] K. Kutschej, P. H. Mayrhofer, M. Kathrein, P. Polcik and C. Mitterer. *Surf. Coat. Technol.* 188-189, 358 (2004).

[48] K. Kutschej, P. H. Mayrhofer, M. Kathrein, P. Polcik and C. Mitterer. *Surf. Coat. Technol.* 200(5-6), 1731 (2005).

[49] R. Franz, J. Neidhardt, B. Sartory, R. Kaindl, R. Tessadri, P. Polcik, V. Derflinger and C. Mitterer. *Tribol. Lett.* 23, 101 (2006).

[50] N. Fateh, G. A. Fontalvo, G. Gassner and C. Mitterer. *Tribol. Lett.* 28, 1 (2007).

[51] N. Fateh, G. A. Fontalvo and C. Mitterer. *Tribol. Lett.* 30, 21 (2008).

[52] K. Kosuge. *J. Phys. Chem. Solids* 28(8), 1613 (1967).

[53] M. J. Ferrante and R. V. Mrazek. High-temperature relative enthalpies of V205. Tech. Rep. 9039, U.S. Bur. Mines Rep. Invest. (1986).

[54] H. A. Wriedt. *J. Phase Equilib.* 10(3), 271 (1989).

[55] G. Gassner, P. H. Mayrhofer, K. Kutschej, C. Mitterer and M. Kathrein. *Surf. Coat. Technol.* 201(6), 3335 (2006).

[56] H. A. Wriedt. *J. Phase Equilib.* 10(4), 368 (1989).

[57] H. P. Kattelus, E. Kolawa, K. Affolter and M.-A. Nicolet. *J. Vac. Sci. Technol. A* 3, 2246 (1985).

[58] E. Kolawa, F. C. T. So, J. L. Tandon and M.-A. Nicolet. *J. Electrochem. Soc.* 134(7), 1759 (1987).

[59] Y. T. Kim, C. W. Lee and S.-K. Min. *Appl. Phys. Lett.* 61(5), 537 (1992).

[60] N. Toyoda, N. Uchitomi, Y. Kitaura, M. Mochizuki, K. Kanazawa, T. Terada, Y. Ikawa and A. Hojo. *IEEE J. Solid-St. Circ.* 20(5), 1043 (1985).

[61] K. Reichelt and G. Bergmann. *J. Appl. Phys.* 46(6), 2747 (1975).

[62] K. J. Huber and C. R. Aita. *J. Vac. Sci. Technol. A* 6(3), 1717 (1988).

[63] J. Lin, A. Tsukune, T. Suzuki and M. Yamada. *J. Vac. Sci. Technol. A* 17(3), 936 (1999).

[64] F. M. Kilbane and P. S. Habig. *J. Vac. Sci. Technol.* 12(1), 107 (1975).

[65] F. C. T. So, E. Kolawa, X.-A. Zhao and M.-A. Nicolet. *Thin Solid Films* 153(1-3), 507 (1987).

[66] L. Boukhris and J.-M. Poitevin. *Thin Solid Films* 310(1-2), 222 (1997).

[67] S. D. Marcus and R. F. Foster. *Thin Solid Films* 236(1-2), 330 (1993).

[68] Y. G. Shen, Y. W. Mai, D. R. McKenzie, Q. C. Zhang, W. D. McFall and W. E. McBride. *J. Appl. Phys.* 88(3), 1380 (2000).

[69] N. M. G. Parreira, N. J. M. Carvalho and A. Cavaleiro. *Mater. Sci. Forum* 514-516, 825 (2006).

[70] A. Magnéli. *Acta Crystallogr.* 6(6), 495 (1953).

[71] A. Magnéli, B. Blomberg-Hansson, L. Kihlborg and G. Sundkvist. *Acta Chem. Scand.* 8, 1382 (1955).

[72] A. D. Wadsley. *Rev. Pure Appl. Chem.* 5, 165 (1955).

[73] L. A. Bursill and B. G. Hyde. *J. Solid State Chem.* 4(3), 430 (1972).

[74] S. Andersson and A. D. Wadsley. *Nature* 211, 581 (1966).

[75] L. Kihlborg, B.-O. Marinder, M. Sundberg, F. Portemer and O. Ringaby. *J. Solid State Chem.* 111(1), 111 (1994).

[76] M. Sundberg and R. J. D. Tilley. *Phys. Status Solidi A* 22(2), 677 (1974).

[77] A. Dietrich, C. R. A. Catlow and B. Maigret. *Mol. Simul.* 11(5), 251 (1993).

[78] J. Stringer. *J. Less-Common Met.* 8, 1 (1965).

[79] H. Katzke, P. Tolédano and W. Depmeier. *Phys. Rev. B* 68(2), 024109 (2003).

[80] L. Fiermans, P. Clauws, W. Lambrecht, L. Vandenbroucke and J. Vennik. *Phys. Status Solidi A* 59(2), 485 (1980).

[81] U. Schwingenschlögl and V. Eyert. *Ann. der Phys.* 13, 475 (2004).

[82] G. Andersson. *Acta Chem. Scand.* 8(9), 1599 (1954).

[83] R. J. D. Tilley and B. G. Hyde. *J. Phys. Chem. Solids* 31(7), 1613 (1970).

[84] P. J. Gellings. In G. Webb and G. C. Bond, eds., *Catalysis*, vol. 7. The Royal Society of Chemistry, London (1985).

[85] J. Haber. *The Role of Molybdenum in Catalysis*. Climax Molybdenum Co Ltd, London (1981).

[86] S. T. Oyama and G. A. Somorjai. *J. Phys. Chem.* 94(12), 5022 (1990).

[87] Z. Zhu, Z. Liu, S. Liu and H. Niu. *Appl. Catal., B* 23(4), L229 (1999).

[88] F. J. Morin. *Phys. Rev. Lett.* 3(1), 34 (1959).

[89] J. B. Goodenough. *Annu. Rev. Mater. Sci.* 1(1), 101 (1971).

[90] J. M. Honig and L. L. V. Zandt. *Annu. Rev. Mater. Sci.* 5(1), 225 (1975).

[91] A. Zylbersztejn and N. F. Mott. *Phys. Rev. B* 11(11), 4383 (1975).

[92] S. Shin, S. Suga, M. Taniguchi, M. Fujisawa, H. Kanzaki, A. Fujimori, H. Daimon, Y. Ueda, K. Kosuge and S. Kachi. *Phys. Rev. B* 41(8), 4993 (1990).

[93] M. Imada, A. Fujimori and Y. Tokura. *Rev. Mod. Phys.* 70(4), 1039 (1998).

[94] U. Schwingenschlögl, V. Eyert and U. Eckern. *Europhys. Lett.* 64(5), 682 (2003).

[95] D. Adler. *Rev. Mod. Phys.* 40(4), 714 (1968).

[96] S. Kachi, K. Kosuge and H. Okinaka. *J. Solid State Chem.* 6, 258 (1973).

[97] P. C. Canfield, J. D. Thompson and G. Gruner. *Phys. Rev. B* 41(7), 4850 (1990).

[98] K. Kawashima, Y. Ueda, K. Kosuge and S. Kachi. *J. Cryst. Growth* 26, 321 (1974).

[99] R.-P. Blum, H. Niehus, C. Hucho, R. Fortrie, M. V. Ganduglia-Pirovano, J. Sauer, S. Shaikhutdinov and H.-J. Freund. *Phys. Rev. Lett.* 99(22), 226103 (2007).

[100] C. Sella, M. Maaza, O. Nemraoui, J. Lafait, N. Renard and Y. Sampeur. *Surf. Coat. Technol.* 98(1-3), 1477 (1998).

[101] W. C. Dautremont-Smith. *Displays* 3(1), 3 (1982).

[102] K.-C. Cheng, F.-R. Chen and J.-J. Kai. *Sol. Energy Mater. Sol. Cells* 90(7-8), 1156 (2006).

[103] S. K. Deb. *Proc. R. Soc. London, Ser. A* 304, 211 (1968).

[104] M. R. Tubbs. *Phys. Status Solidi A* 21(1), 253 (1974).

[105] S. K. Deb. *Philos. Mag.* 27(4), 801 (1973).

[106] K. Bange and T. Gambke. *Adv. Mater.* 2(1), 10 (1990).

[107] C. O. Avellaneda and L. O. S. Bulhões. *Solid State Ionics* 165(1-4), 117 (2003).

[108] B. K. Chakraverty, M. J. Sienko and J. Bonnerot. *Phys. Rev. B* 17(10), 3781 (1978).

[109] M. S. Whittingham. *Chem. Rev.* 104(10), 4271 (2004).

[110] P. Patnaik. *Handbook of inorganic chemicals*. McGraw-Hill, New York (2002).

[111] A. Erdemir. *Tribol. Lett.* 8, 97 (2000).

[112] G. Kresse, S. Surnev, M. G. Ramsey and F. P. Netzer. *Surf. Sci.* 492, 329 (2001).

[113] A. Chakrabarti, K. Hermann, R. Druzinic, M. Witko, F. Wagner and M. Petersen. *Phys. Rev. B* 59(16), 10583 (1999).

[114] K. Hermann, M. Witko, R. Druzinic, A. Chakrabarti, B. Tepper, M. Elsner, A. Gorschluter, H. Kuhlenbeck and H. J. Freund. *J. Electron Spectrosc. Relat. Phenom.* 98-99, 245 (1999).

[115] V. Brázdová, M. V. Ganduglia-Pirovano and J. Sauer. *Phys. Rev. B* 69(16), 165420 (2004).

[116] M. V. Ganduglia-Pirovano and J. Sauer. *Phys. Rev. B* 70(4), 045422 (2004).

[117] A. Magnéli. *Acta Chem. Scand.* 11, 28 (1957).

[118] A. Magnéli. *Acta Chem. Scand.* 2, 861 (1948).

[119] A. Magnéli and B. M. Oughton. *Acta Chem. Scand.* 5, 581 (1951).

[120] T. Vogt, P. M. Woodward and B. A. Hunter. *J. Solid State Chem.* 144(1), 209 (1999).

[121] K. R. Locherer, I. P. Swainson and E. K. H. Salje. *J. Phys.: Condens. Matter* 11(21), 4143 (1999).

[122] A. Aird, M. C. Domeneghetti, F. Mazzi, V. Tazzoli and E. K. H. Salje. *J. Phys.: Condens. Matter* 10(33), L569 (1998).

[123] E. Salje. *Acta Crystallogr. Sect. B* 33(2), 574 (1977).

[124] K. Meisel. *Z. Anorg. Allg. Chem.* 207(1), 121 (1932).

[125] R. Enjalbert and J. Galy. *Acta Crystallogr. Sect. C* 42(11), 1467 (1986).

[126] R. E. Newnham and Y. M. de Haan. *Z. Kristallogr.* 117, 235 (1962).

[127] S. Westman. *Acta Chem. Scand.* 15, 217 (1961).

[128] T. Ohno, Y. Nakamura and S. Nagakura. *J. Solid State Chem.* 56, 318 (1985).

[129] J. Darriet and J. Galy. *J. Solid State Chem.* 4, 357 (1972).

[130] H. Hartmann and W. Mässing. *Z. Anorg. Allg. Chem.* 266(1-3), 98 (1951).

[131] K. A. Wilhelmi and K. Waltersson. *Acta Chem. Scand.* 24, 3409 (1970).

[132] E. Schrödinger. *Phys. Rev.* 28, 1049 (1926).

[133] W. Kohn. In E. I. Grenthe, ed., *Nobel Lectures, Chemistry, 1996–2000*. World Scientific Publishing Co., Singapore (1999).

[134] P. Hohenberg and W. Kohn. *Phys. Rev.* 136(3B), B864 (1964).

[135] D. R. Hartree. *Math. Proc. Cambridge Philos. Soc.* 24, 89 (1928).

[136] D. R. Hartree. *Math. Proc. Cambridge Philos. Soc.* 24, 111 (1928).

[137] V. Fock. *Z. Phys. A: Hadrons Nucl.* 61, 126 (1930).

[138] W. Kohn and L. J. Sham. *Phys. Rev.* 140(4A), A1133 (1965).

[139] J. P. Perdew and Y. Wang. *Phys. Rev. B* 45(23), 13244 (1992).

[140] O. Eriksson. In *Encyclopedia of materials: Science and technology updates*, pp. 1–11. Elsevier Science Ltd., Oxford (2004).

[141] D. Vanderbilt. *Phys. Rev. B* 41, 7892 (1990).

[142] G. Kresse and D. Joubert. *Phys. Rev. B* 59(3), 1758 (1999).

[143] P. E. Blöchl. *Phys. Rev. B* 50(24), 17953 (1994).

[144] H. J. Monkhorst and J. D. Pack. *Phys. Rev. B* 13(12), 5188 (1976).

[145] M. C. Neuburger. *Z. Kristallogr.* 93, 314 (1936).

[146] L. E. Sutton. *Table of Interatomic Distances and Configuration in Molecules and Ions, Supplement 1956–1959*. Special Publication No. 18. The Chemical Society, London (1965).

[147] F. Birch. *J. Geophys. Res.* 83, 1257 (1978).

[148] S. F. Pugh. *Philos. Mag.* 45, 823 (1954).

[149] L. Vitos, P. A. Korzhavyi and B. Johansson. *Nat. Mater.* 2, 25 (2003).

[150] D. R. Lide, ed. *CRC Handbook of Chemistry and Physics*. CRC Press/Taylor and Francis Group, Boca Raton, FL., 86th edn. (2005). Taylor & Francis.

[151] D. C. Wallace. *Thermodynamics of Crystals*. John Wiley and Sons, New York (1972).

[152] M. J. Mehl, J. E. Osburn, D. A. Papaconstantopoulos and B. M. Klein. *Phys. Rev. B* 41(15), 10311 (1990).

[153] M. J. Mehl, B. M. Klein and D. A. Papaconstantopoulos. In J. H. Westbrook and R. L. Fleischer, eds., *Intermetallic Compounds: Principles and Applications*. John Wiley and Sons Ltd., London (1994).

[154] P. Ravindran, L. Fast, P. A. Korzhavyi, B. Johansson, J. Wills and O. Eriksson. *J. Appl. Phys.* 84, 4891 (1998).

[155] L. Fast, J. M. Wills, B. Johansson and O. Eriksson. *Phys. Rev. B* 51(24), 17431 (1995).

[156] R. Snyders, D. Music, D. Sigumonrong, B. Schelnberger, J. Jensen and J. M. Schneider. *Appl. Phys. Lett.* 90(19), 193902 (2007).

[157] D. Music, Z. Sun and J. M. Schneider. *Solid State Commun.* 137, 306 (2006).

[158] K. Albe. *Phys. Rev. B* 55(10), 6203 (1997).

[159] N. Ooi, A. Rairkar and J. B. Adams. *Carbon* 44, 231 (2006).

[160] K. Momma and F. Izumi. *J. Appl. Crystallogr.* 41(3), 653 (2008).

[161] C. L. Fu. *J. Mater. Res.* 5(5), 971 (1990).

[162] P. Lazar and R. Podloucky. *Phys. Rev. B* 73(10), 104114 (2006).

[163] D. L. Smith. *Thin-film deposition: Principles and practice*. McGraw-Hill, New York (1995).

[164] W. D. Westwood. *Sputter Deposition*. AVS Education Committee book series. AVS, New York (2003).

[165] B. Chapman. *Glow Discharge Processes: Sputtering and Plasma Etching*. John Wiley & Sons, New York (1980).

[166] H. N. G. Wadley, W. Zou, X. W. Zhou, J. F. Groves, S. Desa, R. Kosut, E. Abrahamson, S. Ghosal, A. Kozak and D. X. Wang. *Mater. Res. Soc. Symp. Proc.* 538, 323 (1999).

[167] M. Ohring. *The Materials Science of Thin Films*. Academic Press, San Diego (1992).

[168] P. Sigmund. *Phys. Rev.* 184(2), 383 (1969).

[169] A. Matthews. *J. Vac. Sci. Technol. A* 21(5), S224 (2003).

[170] C. Steinbrüchel. *Appl. Phys. A: Mater. Sci. Process.* 36, 37 (1985).

[171] W. D. Wilson, L. G. Haggmark and J. P. Biersack. *Phys. Rev. B* 15(5), 2458 (1977).

[172] N. Matsunami, Y. Yamamura, Y. Itikawa, N. Itoh, Y. Kazumata, S. Miyagawa, K. Morita and R. Shimizu. *Radiation Effects* 57(1), 15 (1980).

[173] Y. Yamamura and S. Shindo. *Radiation Effects* 80(1), 57 (1984).

[174] P. C. Zalm. *J. Vac. Sci. Technol. B* 2(2), 151 (1984).

[175] S. Bhattacharjee, J. Zhang, V. Shutthanandan, P. K. Ray, N. R. Shivaparan and R. J. Smith. *Nucl. Instrum. Methods Phys. Res., Sect. B* 129(1), 123 (1997).

[176] I. Petrov, L. Hultman, U. Helmersson, J.-E. Sundgren and J. E. Greene. *Thin Solid Films* 169(2), 299 (1989).

[177] I. Petrov, L. Hultman, J.-E. Sundgren and J. E. Greene. *J. Vac. Sci. Technol. A* 10(2), 265 (1992).

[178] T. Larsson, H.-O. Blom, C. Nender and S. Berg. *J. Vac. Sci. Technol. A* 6(3), 1832 (1988).

[179] S. Schiller, G. Beister and W. Sieber. *Thin Solid Films* 111(3), 259 (1984).

[180] D. Depla and R. D. Gryse. *Plasma Sources Sci. Technol.* 10(4), 547 (2001).

[181] S. Maniv and W. D. Westwood. *J. Vac. Sci. Technol.* 17(3), 743 (1980).

[182] S. Kadlec, J. Musil and H. Vyskocil. *J. Phys. D: Appl. Phys.* 19(9), L187 (1986).

[183] D. K. Hohnke, D. J. Schmatz and M. D. Hurley. *Thin Solid Films* 118(3), 301 (1984).

[184] I. Petrov, A. Myers, J. E. Greene and J. R. Abelson. *J. Vac. Sci. Technol. A* 12(5), 2846 (1994).

[185] J. Bohlmark, M. Östbye, M. Lattemann, H. Ljungcrantz, T. Rosell and U. Helmersson. *Thin Solid Films* 515(4), 1928 (2006).

[186] J. M. Schneider, W. D. Sproul, A. A. Voevodin and A. Matthews. *J. Vac. Sci. Technol. A* 15(3), 1084 (1997).

[187] J. M. Schneider, S. Rohde, W. D. Sproul and A. Matthews. *J. Phys. D: Appl. Phys.* 33(18), R173 (2000).

[188] V. Kouznetsov, K. Macák, J. M. Schneider, U. Helmersson and I. Petrov. *Surf. Coat. Technol.* 122(2-3), 290 (1999).

[189] K. Sarakinos, J. Alami and S. Konstantinidis. *Surf. Coat. Technol.* 204(11), 1661 (2010).

[190] K. Macák, V. Kouznetsov, J. M. Schneider, U. Helmersson and I. Petrov. *J. Vac. Sci. Technol. A* 18(4), 1533 (2000).

[191] A. P. Ehiasarian, R. New, W.-D. Münz, L. Hultman, U. Helmersson and V. Kouznetsov. *Vacuum* 65(2), 147 (2002).

[192] W. M. Posadowski and A. Brudnik. *Vacuum* 53(1-2), 11 (1999).

[193] D. J. Christie. *J. Vac. Sci. Technol. A* 23(2), 330 (2005).

[194] A. Anders, J. Andersson and A. P. Ehiasarian. *J. Appl. Phys.* 102(11), 113303 (2007).

[195] J. Emmerlich, S. Mráz, R. Snyders, K. Jiang and J. M. Schneider. *Vacuum* 82(8), 867 (2008).

[196] S. Konstantinidis, J. P. Dauchot, M. Ganciu and M. Hecq. *Appl. Phys. Lett.* 88(2), 021501 (2006).

[197] D. Lundin, P. Larsson, E. Wallin, M. Lattemann, N. Brenning and U. Helmersson. *Plasma Sources Sci. Technol.* 17(3), 035021 (2008).

[198] L. Reimer and G. Pfefferkorn. *Raster-Elektronenmikroskopie*. Springer-Verlag, Berlin, 2nd edn. (1977).

[199] J. Goldstein, D. E. Newbury, D. C. Joy, C. E. Lyman, P. Echlin, E. Lifshin, L. Sawyer and J. R. Michael. *Scanning Electron Microscopy and X-ray Microanalysis*. Springer, 3rd edn. (2003).

[200] W. Borchert-Ott. *Kristallographie: Eine Einführung für Naturwissenschaftler*. Springer-Verlag, Berlin Heidelberg, 5th edn. (1997).

[201] B. D. Cullity and S. R. Stock. *Elements of X-ray diffraction*. Addison Wesley Publishing Company, Inc., Massachusetts, USA, 2nd edn. (1978).

[202] A. C. Fischer-Cripps. *Vacuum* 58(4), 569 (2000).

[203] E. S. Berkovich. *Ind. Diamond Rev.* 11(127), 129 (1951).

[204] W. C. Oliver and G. M. Pharr. *J. Mater. Res.* 7, 1564 (1992).

[205] D. Vodnick. Nanomechanical Characterization of Coatings. Tech. rep., Paint & Coatings Industry (2006).

[206] M. D. Banus, T. B. Reed and A. J. Strauss. *Phys. Rev. B* 5(8), 2775 (1972).

[207] D. Watanabe, B. Andersson, J. Gjønnes and O. Terasaki. *Acta Crystallogr. Sect. A* 30(6), 772 (1974).

[208] M. Morinaga and J. B. Cohen. *Acta Crystallogr. Sect. A* 32(3), 387 (1976).

[209] J. H. Gieske and G. R. Barsch. *Phys. Stat. Sol.* 29(1), 121 (1968).

[210] D. G. Isaak, J. D. Carnes, O. L. Anderson, H. Cynn and E. Hake. *Phys. Chem. Miner.* 26, 31 (1998).

[211] C. Kittel. *Introduction to Solid State Physics*. John Wiley and Sons, New York, 7th edn. (1996).

[212] B. Holm, R. Ahuja and B. Johansson. *Appl. Phys. Lett.* 79, 1450 (2001).

[213] D. Music, Z. Sun, A. A. Voevodin and J. M. Schneider. *Solid State Commun.* 139, 139 (2006).

[214] D. Music, A. Houben, R. Dronskowski and J. M. Schneider. *Phys. Rev. B* 75(17), 174102 (2007).

[215] T. Reeswinkel, D. G. Sangiovanni, V. Chirita, L. Hultman and J. M. Schneider. *Surf. Coat. Technol.* 205(20), 4821 (2011).

[216] J. F. Ziegler, J. P. Biersack and M. D. Ziegler. *The stopping and range of ions in solids*, vol. 1. Pergamon Press, New York (1985).

[217] J. F. Yang, Z. G. Yuan, G. G. Zhang, X. P. Wang and Q. F. Fang. *Mater. Res. Bull.* 44(10), 1948 (2009).

[218] Y. G. Shen and Y. W. Mai. *Mater. Sci. Eng. A* 288(1), 47 (2000).

[219] O. Knotek, R. Elsing, G. Krämer and F. Jungblut. *Surf. Coat. Technol.* 46(3), 265 (1991).

[220] V. Valvoda, A. J. Perry, L. Hultman, J. Musil and S. Kadlec. *Surf. Coat. Technol.* 49(1-3), 181 (1991).

[221] D. V. Suetin, I. R. Shein and A. L. Ivanovskii. *Phys. Status Solidi B* 245(8), 1590 (2008).

[222] P. H. Mayrhofer, D. Music, T. Reeswinkel, H.-G. Fuß and J. M. Schneider. *Acta Mater.* 56(11), 2469 (2008).

[223] J. H. Moser, F. Tian, O. Haller, D. B. Bergstrom, I. Petrov, J. E. Greene and C. Wiemer. *Thin Solid Films* 253(1-2), 445 (1994).

[224] T. Polcar, N. M. G. Parreira and A. Cavaleiro. *Wear* 265(3-4), 319 (2008).

[225] D. G. Sangiovanni, V. Chirita and L. Hultman. *Phys. Rev. B* 81(10), 104107 (2010).

[226] K. Chen, L. R. Zhao, J. Rodgers and J. S. Tse. *J. Phys. D: Appl. Phys.* 36(21), 2725 (2003).

[227] K. M. Wong, Y. G. Shen and P. L. Wong. *Sci. China, Ser. A* 44, 242 (2001).

[228] K. K. Shih, D. A. Smith and J. R. Crowe. *J. Vac. Sci. Technol. A* 6(3), 1681 (1988).

[229] Y. P. Purandare, A. P. Ehiasarian, M. M. Stack and P. E. Hovsepian. *Surf. Coat. Technol.* 204(8), 1158 (2010).

[230] A. Guillaumot, F. Lapostolle, C. Dublanche-Tixier, J. C. Oliveira, A. Billard and C. Langlade. *Vacuum* 85(2), 120 (2010).

[231] J. Lin, J. J. Moore, W. D. Sproul, B. Mishra, Z. Wu and J. Wang. *Surf. Coat. Technol.* 204(14), 2230 (2010).

Appendix A

Ab initio calculation methods applied for nitrides

The Vienna ab initio simulation package (VASP) [142] was used to perform DFT calculations in the generalized-gradient approximation of Perdew-Wang (GGA-PW91) [139]. All electron–ion interactions were described by the projector augmented wave potentials (PAW) [143] and the total energy was minimised to achieve convergence within 10×10^{-5} eV by using a large energy cutoff of 500 eV for the plane-wave basis. To maintain high accuracy in the structure relaxations $4 \times 4 \times 4$ k-points grids have been used to sample the Brillouin zone with the Monkhorst-Pack scheme [144]. All calculations were performed on supercells containing 64 atoms, with a cubic B1 structure, for $Ti_{0.5-x}Al_{0.5-x}W_{2x}N$ alloys with $0 \leq x \leq 0.375$. Lattice constants a and bulk moduli B were calculated by minimising the total energy and fitting the energy–volume curve to the Birch-Murnaghan equation of state [147]. The methods used for calculating the elastic constants and related moduli have been published recently [225]. In addition, the effect of N vacancies on the bulk properties of two quaternary nitrides have been assessed, $Ti_{0.125}Al_{0.125}W_{0.75}N_{0.875}$ and $Ti_{0.125}Al_{0.125}W_{0.75}N_{0.75}$. In this case, the optimal geometry was found by minimising the total energy while allowing for simultaneous cell shape and atomic positions relaxations, resulting in a triclinic primitive cell with similar lattice parameters and angles close to $\pi/2$. Subsequently, the elastic constants and moduli of these quasi-cubic structures were estimated using the scheme employed for cubic alloys. In the case of stoichiometric alloys, and for all x values, changing the atomic arrangement on the metal sites induces small variations in the elastic properties (within 3 %). It can be concluded that the effect of varying atomic distributions in supercells is indeed negligible. Consequently, the single condition imposed on the atomic configurations used herein was to fulfil the minimum requirement for symmetry in cubic systems: invariance with respect to rotations of $\pm 2\pi/3$ about axes in the $\langle 111 \rangle$ directions.